Statistical characteristics of raindrop size distribution over Western Ghats of India: wet versus dry spells of Indian Summer Monsoon

Uriya Veerendra Murali Krishna[1], Subrata Kumar Das[1], Ezhilarasi Govindaraj Sulochana[2], Utsav Bhowmik[1], Sachin Madhukar Deshpande[1], and Govindan Pandithurai[1]

[1]Indian Institute of Tropical Meteorology, Ministry of Earth Sciences, Pashan, Pune 411008, India
[2]College of Engineering, Guindy, Chennai 600025, India

Correspondence: Subrata Kumar Das (skd_ncu@yahoo.com)

Abstract. The nature of raindrop size distribution (DSD) is analyzed for wet and dry spells of Indian Summer Monsoon (ISM) in the Western Ghats (WGs) region using Joss-Waldvogel Disdrometer (JWD) measurements during ISM period (June-September) in 2012-2015. The observed DSDs are fitted with gamma distribution. Observations show a higher number of smaller drops in dry spells and more mid-size and large drops in wet spells. The DSD spectra show distinct diurnal variation during wet and dry spells. The dry spells exhibit a strong diurnal cycle with two peaks, while the diurnal cycle is not very prominent in the wet spells. Results reveal the microphysical characteristics of warm rain during both wet and dry periods. However, the underlying dynamical parameters such as moisture availability, vertical wind, etc. cause the differences in DSD characteristics. The higher moisture and strong vertical winds can provide sufficient time for the raindrops to grow bigger in wet spells, whereas the higher temperature may lead to evaporation and drop breakup processes in dry spells. In addition, the differences in DSD spectra with different rain rates are also observed. The DSD spectra are further analyzed by separating into stratiform and convective rain types. Finally, an empirical relationship between slope parameter, λ and shape parameter, μ is derived by fitting the quadratic polynomial during wet and dry spells as well as for stratiform and convective types of rain. The $\mu-\lambda$ relations obtained in this work are slightly different compared to previous studies. These differences could be related to different rain microphysics such as collision-coalescence, breakup, etc.

Keywords. Raindrop size distribution, Wet and dry spells, Monsoon, Western Ghats, Disdrometer

1 Introduction

Western Ghats (WGs) is one of the heavy rainfall regions in India. WGs receives a large amount of rainfall ($\sim$ 6000 mm) during the Indian Summer Monsoon (ISM) period (Das et al., 2017, and references therein). Shallow convection contribute significantly to the monsoon rainfall on the windward side (Kumar et al., 2014; Das et al., 2017; Utsav et al., 2017, 2019) and deep convection in the leeward side (Utsav et al., 2017, 2019; Maheskumar et al., 2014) of WGs. The rainfall distribution in WGs region is complex in which topography plays a significant role (Houze, 2012, and references therein). The rainfall distribution on WGs depend on the area, whether on the mountain's windward or leeward side. For instance, Varikoden et al. (2019) showed that the rainfall trends are different in northern and southern parts of the WG. These different properties correspond to

different physical mechanisms. The intense rainfall in WGs windward side, usually called the orographic precipitation, comes from shallow clouds with long-lasting convection (Das et al., 2017; Utsav et al., 2017, 2019).

The ISM rainfall shows large spatial and temporal variability. It is known that during active (with a high amount of rainfall) and break (with a little or no rain) spells of ISM, there are different behaviours in the formation of weather systems and large-scale instability. The strength of ISM rainfall depends on the frequency and duration of active and break spells (Kulkarni et al., 2011). This intra-seasonal oscillation of rainfall is considered one of the most critical weather variability sources in the Indian region (Hoyos and Webster, 2007). From the earlier studies of Ramamurthy (1969), active and break spells of ISM have been extensively studied, especially during the last two decades (Goswami and Mohan, 2001; Gadgil and Joseph, 2003; Uma et al., 2012; Satyanarayana Mohan and Narayana Rao, 2012; Rajeevan et al., 2013; Das et al., 2013; Rao et al., 2016). The characteristic features of ISM active and break spells have been widely reported in earlier studies; for example, their identification (Rajeevan et al., 2006, 2010), spatial distribution (Ramamurthy, 1969; Rajeevan et al., 2010), circulation patterns (Goswami and Mohan, 2001; Rajeevan et al., 2010), vertical wind and thermal structure (Uma et al., 2012), rainfall variability (Deshpande and Goswami, 2014; Rao et al., 2016) and cloud properties (Rajeevan et al., 2013; Das et al., 2013). Even though different dynamical mechanisms for the observed rainfall distribution during wet and dry spells of ISM are well understood, the investigation on microphysical processes for rain formation is still lacking.

Raindrop size distribution (DSD) is a fundamental microphysical property of precipitation. The DSD characteristics are related to processes such as hydrometeor condensation, coalescence, and evaporation. In addition, the altitudinal variations in DSD parameters provide the cloud and rain microphysical processes (Harikumar et al., 2012). These are important parameters affecting the microphysical processes in the parameterization schemes of numerical models (Gao et al., 2011). Hence, numerous DSD observations during different types of precipitation, different seasons, and different intra-seasonal periods at several locations are essential for better representation of physical processes in the parameterization schemes. As a result, the numerical model communities continue to improve the simulation of clouds and precipitation at the monsoon intra-seasonal scales by better representing the microphysical processes through parameterization schemes. In addition, different DSD characteristics lead to different reflectivity (Z) and rainfall rate (R) relations. Henceforth, understanding DSD variability is also vital to improve the quantitative precipitation estimation's reliability and accuracy from radars and satellites (Rajopadhyaya et al., 1998; Atlas et al., 1999; Viltard et al., 2000; Ryzhkov et al., 2005).

The ISM active and break spells over WGs are nearly identical with active and break phases over the core monsoon zone (Gadgil and Joseph, 2003). The distribution of convective clouds in the WGs region exhibits distinct spatiotemporal variability at intra-seasonal time scales (wet: analogous to active period of ISM and dry: similar to break period of ISM) during the ISM. Recently, Utsav et al. (2019) studied the characteristics of convective clouds over WGs using X-band radar, European Center for Medium-range Weather Forecasting (ECMWF) interim reanalysis (ERA-Interim), and Tropical Rainfall Measuring Mission (TRMM) satellite datasets. They showed that the wet spells are associated with negative geopotential height anomalies at 500 hPa, negative outgoing long-wave radiation (OLR) anomalies, and positive precipitable water anomalies. All these features promote the anomalous south-westerlies, which enhances convective activity over WGs. In contrast, positive geopotential height anomalies, positive OLR anomalies, and negative precipitable water anomalies are observed during the dry spells,

which suppress the convective activity in the Arabian Sea, and hence little to no rain is seen over WGs during dry periods. These different dynamical properties affect the convection during wet and dry spells over WGs. However, DSD (often used to infer the microphysical processes of rain) during wet and dry ISM periods is least addressed, especially in the WGs region.

Several studies demonstrated the seasonal variations in DSD over Indian region (e.g., Reddy and Kozu, 2003; Harikumar et al., 2009; Konwar et al., 2014; Harikumar, 2016; Das et al., 2017; Lavanya et al., 2019). However, the climatological studies of DSD over orographic regions are limited, especially in the WGs region. Despite its orography, the rainfall intensity is less (below 10 $\mathrm{mm\,h^{-1}}$) over WGs (Kumar et al., 2007; Das et al., 2017). A few attempts have been made to understand the DSD characteristics in WGs. For example, Konwar et al. (2014) studied the DSD characteristics by fitting three-parameter gamma function during monsoon. They observed a bimodal and monomodal DSD during low and high rainfall rates, respectively. However, their study is limited to brightband and non-brightband conditions only. Harikumar (2016) examined the DSD differences between coastal (Kochi) and high altitude (Munnar) stations located in the WGs region and reported larger drops are relatively higher at Munnar. Das et al. (2017) studied the DSD characteristics during different precipitating systems in the WGs region using disdrometer, Micro Rain Radar, and X-band radar measurements. They noticed different *Z-R* relations for different precipitating systems. Sumesh et al. (2019) studied the DSD differences between mid- (Braemore, 0.4 km above mean sea level) and high-altitude (Rajamallay, 1.8 km above mean sea level) regions in southern WGs during brightband events. They observed bimodal DSD in the mid-altitude station and monomodal DSD in the high-altitude station. However, their study confined to stratiform rain only.

The DSD studies are inadequate in the WGs region by considering long-term dataset. This work is the first to analyze the DSD characteristics and plausible dynamic and microphysical processes by considering the monsoon intra-seasonal oscillations (wet and dry spells). The present study brings out the results of a unique opportunity by analyzing a more extensive dataset and considering different phases of monsoon intra-seasonal oscillations in the WGs. With this background, the current study attempt to address the following issues over WGs:

(i) How DSD characteristics vary during wet and dry spells?

(ii) Does wet and dry spell rainfall have different microphysical origin over the complex terrain?

(iii) Does DSD show any diurnal differences like in rainfall distribution during wet and dry spells?

(iv) What are the dynamical processes influencing DSD characteristics during wet and dry spells?

(v) Establish the best fit for $\mu-\lambda$ relationships during wet and dry spells.

The paper is organized as follows: details of the instrument and dataset used are presented in section 2. The methodology adopted for separating rainy days into wet and dry spells is given in section 3. A brief overview of DSD variation with topography is in section 4. The characteristics of DSDs during wet and dry spells and the possible reasons are reported in section 5. The summary of this study is provided in section 6.

2 Instrument and Datasets

Four years (June to September; 2012-2015) Joss-Waldvogel Disdrometer (JWD) measurements at High Altitude Cloud Physics Laboratory (HACPL; located in the windward slopes of the WGs), Mahabaleshwar (17.92° N, 73.6° E, $\sim$1.4 km above mean sea level) is utilized to understand the DSD variations during wet and dry spells of ISM. Figure 1 shows the topography map along with the disdrometer site (HACPL). The background surface meteorological parameters like temperature, relative humidity, rainfall accumulation, wind speed, and wind direction measured with automatic weather station over the study site can be found in Das et al. (2020).

JWD is an impact type disdrometer, which measures the hydrometeors with sizes ranging from 0.3 to 5.1 mm and arranges them in 20 channels (Joss and Waldvogel, 1969). The JWD has styrofoam cone to measure the diameter of hydrometeors. Once the hydrometeors hit 50 cm^2 styrofoam cone, a voltage is induced by downward displacement, which is directly correlated with drop size. The accuracy of JWD is 5% of the measured drop diameter. Although JWD is a standard instrument for DSD measurements (Tokay et al., 2005), it has several shortcomings, such as noise, sampling errors, wind, etc. (Tokay et al., 2001, 2003). In addition, JWD miscounts raindrops in lower-sized bins, specifically for drop diameters below 1 mm (Tokay et al., 2003). An effort has been made to overcome this deficiency by discarding noisy measurements and applying the manufacturer's error correction matrix. To reduce the sampling error arising from insufficient drop counts, the rain rates less than 0.1 $\mathrm{mm\,h^{-1}}$ are discarded. During heavy rain, JWD underestimates the number of smaller drops, known as disdrometer dead time. To account the aforementioned error in JWD estimates, the rain rates during wet and dry spells are analyzed. It is observed that $\sim$85% (90%) of the rain rates lies below 8 $\mathrm{mm\,h^{-1}}$ during wet (dry) spells (figure not shown). Using the noise-limit diagram of Joss and Gori (1976), Tokay et al. (2001) investigated the underestimation of small drops by JWD. They found that 50% of the drops below 0.4 mm cannot be detected by JWD when the rain rate is above 20 $\mathrm{mm\,h^{-1}}$. Here, only 4% (1%) of the rain rates exceed 20 $\mathrm{mm\,h^{-1}}$ during wet (dry) spells, and hence, the underestimation of small drops by JWD is negligible in this region. Tokay et al. (2001) further demonstrated that the gamma parameters (such as normalized intercept parameter etc.) derived from long-term observations by JWD and two-dimensional video disdrometer (2DVD) are in good agreement. We examined the DSD differences between the ISM's wet and dry spells using long-term (four monsoon) dataset in the present study. So it is appropriate that the undercounting of small drops do not significantly affect the gamma DSD. Further, the underestimation of smaller drops for higher rain rate (4% for wet spells and 1% for dry spells) may not affect the conclusions, as this work does not intend to quantify the DSD variations. Instead, it aims to understand the DSD variability during wet and dry spells over the complex terrain. The undersized integration period can contribute to DSD's numerical fluctuations, whereas higher sampling time may miscount actual physical deviations (Testud et al., 2001). As there is no consensus regarding JWD sampling period, we have averaged JWD measurements into 1-min period to filter out these deviations.

JWD provides rain integral parameters, like, raindrop concentration, rain rate, reflectivity, etc. at 1-min integration time (Krishna et al., 2016; Das et al., 2017). The 1-min DSD measurements are fitted with a three-parameter gamma distribution, as mentioned in Ulbrich (1983). The details about DSDs used in the present study can be found in Das et al. (2017) and Murali Krishna et al. (2017).

The functional form of gamma distribution assumed for DSD is expressed as

$$N(D) = N_0 D^{\mu} exp\Big[-(3.67+\mu)\frac{D}{D_0}\Big] \tag{1}$$

where, N(D) is the number of drops per unit volume per unit size interval, N_0 (in $\mathrm{m^{-3}\,mm^{-(1+\mu)}}$) is the number concentration parameter, D (in mm) is the drop diameter, D_0 (in mm) is the median volume diameter, and μ (unitless) is the shape parameter (Ulbrich, 1983; Ulbrich and Atlas, 1984). The gamma DSD parameters are calculated using moments proposed by Cao and Zhang (2009). Here, 2nd, 3rd, and 4th moments are utilized to estimate gamma parameters. This method gives relatively fewer errors than other methods over WGs (Konwar et al., 2014). The *'n'* order moment of gamma distribution can be calculated as

$$M_n = \int_0^{\infty} D^n N(D) dD \tag{2}$$

The shape parameter, μ, and the slope parameter, λ are expressed as

$$\mu = \frac{1}{1-G} - 4 \tag{3}$$

$$\lambda = \frac{M_2}{M_3}(\mu+3) \tag{4}$$

$$G = \frac{M_3^2}{M_2 M_4} = \frac{\Big[\int_0^{\infty} D^3 N(D) dD\Big]^2}{\Big[\int_0^{\infty} D^2 N(D) dD\Big]\Big[\int_0^{\infty} D^4 N(D) dD\Big]} \tag{5}$$

The other parameters, normalized intercept parameter, N_w (in $\mathrm{mm^{-1}\,m^{-3}}$), mass-weighted mean diameter, D_m (in mm), and liquid water content, *LWC* (in $\mathrm{gm\,m^{-3}}$), are calculated following Bringi and Chandrasekar (2001).

$$D_m = \frac{\int_0^{\infty} D^4 N(D) dD}{\int_0^{\infty} D^3 N(D) dD} \tag{6}$$

$$LWC = 10^{-3}\frac{\pi}{6}\rho_w \int_0^{\infty} D^3 N(D) dD \tag{7}$$

$$N_w = \frac{4^4}{\pi \rho_w}\Big(\frac{10^3 LWC}{D_m^4}\Big) \tag{8}$$

where, ρ_w is the density of water.

Apart from JWD measurements, the ERA-Interim (Dee et al., 2011) dataset is also used to understand the dynamical processes influencing different DSD characteristics. The ERA-Interim provides atmospheric data at different pressure and time

intervals. Here, temperature (K), specific humidity ($\mathrm{kg\,kg^{-1}}$), horizontal and vertical winds at 850 hPa with a spatial resolution of 0.25°× 0.25°at 0000 UTC are considered during ISM period of 2012-2015.

The daily accumulated rainfall collected by the India Meteorological Department (IMD) rain gauges is used to identify ISM's wet and dry spells. IMD receives the rainfall accumulations at 08:30 LT (LT=UTC+05:30 h) every day. To examine JWD data quality, the daily accumulated rainfall measured by JWD is compared with the daily accumulated rainfall collected from rain gauge. For comparison, JWD rainfall data accumulated at 08:30 LT is calculated for all the days during 2015 monsoon. The daily accumulated rainfall collected by rain gauge and JWD above 1 mm is considered for the comparison. A total of 76 days of data is utilized. The non-availability of data might occur either due to maintenance activity or due to non-rainy days. Figure 2 shows the scatter plot of daily accumulated rainfall between JWD and rain gauge. The correlation coefficient is about 0.99 between the two measurements despite their different physical and sampling characteristics. The JWD measured rainfall bias is about -0.7 mm, and root mean square error is about 2.9 mm. These results suggest that the JWD measurements can be utilized to understand the DSD characteristics during wet and dry spells of ISM in the WGs region.

3 Identification of wet and dry spells

Pai et al. (2014) proposed an objective methodology to identify wet and dry spells of ISM. A long-term (1979-2011), high-resolution (0.25°× 0.25°) gridded daily rainfall data from IMD rain gauge network is used to classify the wet and dry spells of ISM. The area-averaged daily rainfall time series is constructed for HACPL, Mahabaleshwar (17.75-18° N and 73.5-73.75° E) region during monsoon (1st June to 30th September) for four years (2012-2015) as well as for long-term data. The daily average rainfall difference for four monsoon and the daily average of long-term data provides the daily anomalies. The standard deviation of daily average rainfall is calculated from long-term data. The standardized anomaly time series is obtained by normalizing the daily anomalies with corresponding standard deviations.

$$Events = \frac{(\textit{Av. of daily rain} - \textit{Av. of long term rain})}{\textit{St. dev. of daily rain}} \tag{9}$$

These standardized anomaly time series are used to separate the wet and dry spells. A period in this time series is marked as wet (dry) if the standardized anomaly exceeds 0.5 (-0.5) for consecutive three days or more (Utsav et al., 2019). Figure 3 shows the standardized rainfall anomalies calculated using eq. (9). Table 1 shows the number of wet and dry days for the study period. It is observed that there are more dry days during 2012-2015 monsoon, and July has relatively more wet days. A total of 44,640 (149,760) 1-min raindrop spectra are analyzed during wet (dry) days for 2012-2015 ISM.

4 DSD overview-Topographic perspective:

A single point-wise instrument is not sufficient to address the orographic impacts on DSD characteristics. One of the difficulties in studying the effect of orography on DSD properties is the unavailability of many disdrometer measurements in the WG region. Here an overview of DSD characteristics over WGs is shown using Global Precipitation Measurement (GPM) mission satellite products. The GPM level 3 data provides different DSD parameters like D_{m} and N_{w} at a spatial resolution of 0.25°×

0.25°from 60° S to 60° N. The GPM is the first space-borne dual-frequency precipitation radar (DPR) contains Ku-band at ∼13.6 GHz and Ka-band at ∼35.5 GHz. The details of GPM mission can be found in Huffman et al. (2015), and the dataset used can be found in Murali Krishna et al. (2017).

The GPM-DPR estimate D_m, and N_w using dual-frequency ratio (DFR) method. However, the GPM-DPR suffers limitations. The DSD parameterization used in GPM-DPR is the gamma distribution with a constant shape parameter, μ=3 (Liao et al., 2014). The constant 'μ' introduce errors in the retrievals. The retrieval of D_m using DFR method is iterative, and it has two solutions when DFR is less than 0 (Meneghini et al., 1997; Liao et al., 2003; Mardiana et al., 2004). The uncertainties in GPM-DPR in estimating DSD are detailed in Seto et al. (2013) and Liao et al. (2014). Murali Krishna et al. (2017) assessed the DSD measurements from GPM in the WGs region by comparing them with ground-based disdrometer. They showed that the seasonal variations in D_m and N_w are well represented in the GPM measurements. However, GPM underestimates D_m and overestimate N_w compared to the ground-based disdrometer. Radhakrishna et al. (2016) also showed GPM underestimates (overestimates) the mean D_m (N_w) during southwest and northeast monsoons over Gadanki, a semiarid region of South India. They showed that the single-frequency algorithm underestimates mean D_m by ~ 0.1 mm below 8 mm h^{-1}, and the underestimation is little higher at higher rain rates. Whereas in DFR algorithm, the mean D_m is nearly the same below 8 mm h^{-1} but underestimates (~ 0.1 mm) at higher rain rates. Further, the underestimation is very small for D_m below 1.5 mm. In most cases, the rainfall intensity is below 8 mm h^{-1} (as discussed in previous section), and D_m is below 1.5 mm in the WGs region. Hence, it is reasonable to consider the GPM measurements to present DSD characteristics over WGs.

Three locations (ocean, windward, and leeward side of WGs) are selected to examine the DSD variations at different topographic regions. The DSD differences in these three sites can partly infer the effect of orography on DSD. Figure 4 shows D_m distribution over ocean, windward, and leeward sides of WGs. The D_m distribution is smaller over ocean and windward sides, whereas D_m shows large variability on the leeward side. Further, D_m median value is low over ocean than windward and leeward sides of the mountain. The smaller distribution of D_m over ocean and windward sides can be attributed to shallow clouds/cumulus congestus. The broader distribution and relatively higher median value of D_m represent the continental convection on the mountain's leeward side. Zagrodnik et al. (2019) also observed narrow D_m distribution during the Olympic Mountains Experiment (OLYMPEX) on the Olympic peninsula's windward side.

5 Results and Discussion

The DSD and rain integral parameters during wet and dry spells are examined in terms of diurnal and with different types of precipitation (convective and stratiform). We considered the raindrops with diameters less than 1 mm as small drops, with diameters between 1 and 4 mm as mid-size drops and with diameters above 4 mm as large drops.

5.1 Raindrop size distribution during wet and dry spells

Figure 5 shows the temporal evolution of normalized raindrop concentration during wet and dry spells for smaller and mid-size drops. The concentration of smaller drops (Figure 5a) is higher during dry periods. The higher concentration of small drops

in dry spells indicates the influence of orography on rainfall over WGs. In the mountain regions rainfall is produced when the upslope wind is stronger, and moisture availability is high (White et al., 2003). In such situation, the strong orographic wind enhances cloud droplet's growth via condensation, collision, and coalescence (Konwar et al., 2014). Further, many small raindrops during dry spells indicate drop breakup and evaporation processes. For smaller drops, dry spells exhibit a strong diurnal cycle with a primary maximum in the afternoon (1500-1900 LT) and a secondary peak in the night (2300-0500 LT). Utsav et al. (2019) also found similar diurnal feature in 15-dBZ echo top height (ETH) from radar observations during the dry spells. However, such a diurnal cycle is not present in smaller drops during wet spells. These smaller drops show a little higher concentration during morning (0500-0700 LT), representing the oceanic nature of rainfall (Narayana Rao et al., 2009; Krishna et al., 2016).

In the mid-size drops (Figure 5b), the concentration is higher in wet than dry spells. The higher concentration of mid-size drops during wet spells could be due to the collision-coalescence process (Rosenfeld and Ulbrich, 2003), and accretion of cloud water by raindrops (Zhang et al., 2008). This result suggests that the congestus clouds are omnipresent during wet spells. A clear diurnal cycle can be observed during both the spells; however, their strengths are different. The wet spells exhibit two broad maxima, one in the late afternoon (1400-1900 LT) and the other in the early morning (0500-0700 LT). The dry spells also show two maxima, one in the late afternoon (1400-1900 LT) as in the wet periods, and the other in the night (2300-0500 LT). Such a diurnal cycle is also observed in rainfall features over WGs (Shige et al., 2017; Romatschke and Houze, 2011). Shige et al. (2017) found a continuous rainfall with a double-peak structure of nocturnal and afternoon-evening maxima in the WGs region. Romatschke and Houze (2011) observed a double peak rainfall pattern in the WGs region. They proposed that the morning peak is related to oceanic convection while the afternoon peak is associated with the continental convection.

Figure 6 shows the mean DSDs during wet and dry spells along with the seasonal mean. Here, $N(\mathrm{D})$ is plotted on a logarithmic scale to accommodate its large variability. In general, the DSDs during dry spells are narrower than wet periods. The DSDs are concave downward during both spells. The mean concentration of smaller drops (below 0.9 mm) is higher, and the mean concentration of medium and larger drops is lower in dry periods. An increased concentration in smaller drops and a decrease in medium and larger drops concentration is found in the dry spells than the seasonal mean concentration. This indicates the collision and breakup processes described by Rosenfeld and Ulbrich (2003) and Konwar et al. (2014). In contrast, low concentrations of smaller drops and an increase in number concentration of drops above 0.9 mm diameter are observed in the wet spells.

To study the differences in DSD during wet and dry spells with rain rate, $N(\mathrm{D})$ distribution is compared at different rain rates, as shown in Figure 7. Here $N(\mathrm{D})$ is plotted on a logarithmic scale. A significant difference in $N(\mathrm{D})$ is found between wet and dry spells. The contours are shifted to higher rain rates and higher diameters in the wet spells. It indicates that the mid-size drops in the range 1-2 mm are higher in wet spells than in dry spells for the same rain rate. This is more pronounced in lower rain rates below 10 $\mathrm{mm\,h^{-1}}$. Further, the raindrop concentration in the range 1-2 mm increases as the rain rate increases between 5 and 15 $\mathrm{mm\,h^{-1}}$ during wet periods. At higher rain rates (above 10 $\mathrm{mm\,h^{-1}}$), the smaller and mid-size drops are higher in the wet spells than in the dry periods. However, this difference decreases gradually as rain rate increases. At above

245 30 $\mathrm{mm\,h^{-1}}$, both the periods show a similar distribution of N(D) (not shown). However, for larger drops above 4.5 mm, the concentration is higher in wet spells than dry periods in all rain rate intervals (not shown).

Figure 8 presents the histograms of D_m, $\log_{10}(N_\mathrm{w})$, λ, and μ during wet and dry spells. The histograms of D_m are positively skewed during both wet and dry periods (Figure 8a). The distribution of D_m is broader in dry spells. The D_m varies from 0.42 to 4.8 mm, with maximum at $\sim$ 1.2 mm during wet periods, whereas it ranges from 0.4 to 5 mm, with maximum at $\sim$ 0.8 mm
250 during dry spells. For D_m below 1 mm, the dry spells distribution is higher than for the wet spells. This finding indicates the predominance of smaller drops during dry spells. The mean, standard deviation and skewness of D_m are provided in Table 2. The mean D_m is 1.3 mm, and its standard deviation is 0.38 during wet spells, whereas the mean D_m is 0.9 mm, and its standard deviation is 0.37 during dry spells. A relatively large number of small drops reduce D_m in dry spells, while fewer smaller drops and relatively more mid-size drops increase D_m in wet periods. The histograms of $\log_{10}(N_\mathrm{w})$ are negatively skewed during
255 both wet and dry spells (Figure 8b). The $\log_{10}(N_\mathrm{w})$ shows an inverse relation with D_m and is varied from 0.52 to 5.11 during wet spells and from 0.50 to 5.43 during dry periods. The histogram of $\log_{10}(N_\mathrm{w})$ peak at 3.9 during wet periods, however, it shows a bimodal distribution during dry spells that peaks at 3.9 and 5. This finding is consistent with Utsav et al. (2019). They analyzed 0-dBZ ETH, which represents the cloud top height and observed a bimodal distribution, which peaks at 3 km and 6.5 km during dry periods. The large standard deviation indicates the large variations in D_m and N_w during both wet and dry
260 periods. The histograms of λ and μ are shown in Figure 8(c)-(d). Generally, λ represents the truncation of DSD tail and μ indicates the breadth of DSD. If λ is small, the DSD tail is extended to larger diameter and vice-versa. The positive (negative) μ indicate the concave downward (upward) shape for the DSD. The zero value of μ represents the exponential shape for DSD (Ulbrich, 1983). The λ shows positive values during wet and dry spells. The occurrence of λ is higher below 10 $\mathrm{mm^{-1}}$ during wet periods, indicating the broader spectrum of raindrops, whereas it is distributed up to 20 $\mathrm{mm^{-1}}$ during dry spells. The
265 extension of λ towards higher values represent the higher occurrence of smaller drops during both periods. Relatively smaller λ and N_w in wet spells indicate that the tail of DSD extends to large raindrop sizes. The μ is positive during both wet and dry spells indicating the concave downward shape of DSD.

Numerous studies have been carried out to understand the DSDs during different types of convection and within a convective system (Dolman et al., 2011; Munchak et al., 2012; Friedrich et al., 2013; Thompson et al., 2015; Dolan et al., 2018). These
270 studies showed the combined dynamical (stratiform and convective) and microphysical processes occurring in a precipitating system cause differences in observed DSD. Therefore, to understand the effect of dynamical processes on different DSD characteristics during wet and dry spells, the precipitation events are classified into stratiform and convective types. Several rain classification schemes proposed in the literature using different instruments, like, disdrometer, radar, profiler (Bringi et al., 2003; Thompson et al., 2015; Krishna et al., 2016; Das et al., 2017; Dolan et al., 2018; Nair, 2019). In this work, the
275 precipitating systems are classified as stratiform and convective based on Bringi et al. (2003) criterion. Even though several other classification schemes are in literature, it is the most widely used classification criterion for stratiform and convective rainfall. The main purpose here is to understand the DSD differences between convective and stratiform (rain which does not come under the convective category) rain systems. For rain type classification, Bringi et al. (2003) considered 5 consecutive 2-min DSD samples. However, 10 successive 1-min DSD samples are considered to classify the rainfall as stratiform and

convective in this work. If the mean rain rate of 10 successive DSD samples is greater than 0.5 $\mathrm{mm\,h^{-1}}$, and if the standard deviation is less than 1.5 $\mathrm{mm\,h^{-1}}$, then the precipitation is classified as stratiform; otherwise, it is classified as convective.

Figure 8(e)-(h) presents the histograms of D_m, $\log_{10}(N_\mathrm{w})$, λ, and μ during stratiform rain events in wet and dry spells. The mean, standard deviation, and skewness of these parameters are provided in Table 3. The histograms of D_m (Figure 8e) are positively skewed during stratiform rain events in both the spells. The D_m is broader in stratiform rain of dry spells and it varies between 0.38 and 2.77 mm with maximum near 0.42-0.58 mm. The distribution of D_m shows higher frequency below 0.6 mm in dry spells. This finding indicates that the presence of more number of smaller raindrops in stratiform rain of dry spells. The D_m varies from 0.42 to 2.48 mm with a maximum near 1-1.4 mm during stratiform rain in wet periods. The D_m distribution is higher in wet spells above 1 mm, indicating the dominance of mid-size and/or larger drops. The histogram of $\log_{10}(N_\mathrm{w})$ (Figure 8f) is positively skewed in the wet spells and negatively skewed in the dry periods for stratiform rain. The distribution is narrower in wet periods and broader in dry spells. The distribution peaks between 3 and 3.6 during wet spells, whereas it peaks at 5 during dry spells. The distribution of λ (Figure 8g) is broader in the stratiform rain events during both wet and dry periods. The distribution varies from 1.2 $\mathrm{mm^{-1}}$ to 52 $\mathrm{mm^{-1}}$ with a mode at 10 $\mathrm{mm^{-1}}$ in the stratiform rain of wet spells. This result further supports the presence of mid-size drops in wet periods. The distribution of λ shows higher occurrences above 15 $\mathrm{mm^{-1}}$ during dry spells, indicating the truncation of DSD at relatively smaller drop diameters. The histograms of μ (Figure 8h) show a concave downward shape for DSDs during stratiform rain events in both wet and dry spells.

Figure 8(i)-(l) shows the distribution of D_m, $\log_{10}(N_\mathrm{w})$, λ, and μ during convective rain events in wet and dry spells. The D_m histograms are positively skewed in convective rain during both wet and dry spells (Figure 8i). In convective rain, the distribution of D_m is broader in wet spells. It can be seen that the presence of small drops is higher in dry spells even in convective rain also. The distribution of $\log_{10}(N_\mathrm{w})$ shows an inverse relation with D_m in convective rain (Figure 8j). The $\log_{10}(N_\mathrm{w})$ is negatively skewed in wet spells, whereas it is positively skewed in dry spells. The distribution of λ (Figure 8k) indicates larger drops in convective rain compared to stratiform rain in both wet and dry spells. The histograms of μ (Figure 8l) show the concave downward shape of DSDs in convective rain of both wet and dry spells. The mean, standard deviation, and skewness of these parameters are provided in Table 4.

Several points can be noted from the above discussion:

a. The maximum value for mean D_m and the largest standard deviation is for convective rain in wet spells.

b. The maximum value for $\log_{10}(N_\mathrm{w})$ and higher standard deviation are observed during stratiform rain in dry spells.

c. A considerable difference is found in D_m and $\log_{10}(N_\mathrm{w})$ during stratiform rain in dry and wet periods. However, this difference is small in convective rain.

d. The distinct differences exist in λ and μ of stratiform rain during wet and dry spells.

The above results indicate that the rainfall over WGs is associated with warm rain processes during wet and dry spells. The microphysical processes in warm rain include rain evaporation, accretion of cloud water by raindrops and rain sedimentation (Zhang et al., 2008). Giangrande et al. (2017) observed the predominance of larger cloud droplets in warm clouds during wet spells over Amazon. Similarly, Machado et al. (2018) showed larger D_m is associated with the mixed-phase clouds during dry periods over Amazon. Recently, Utsav et al. (2019) showed that cumulus congestus is higher during wet spells, and shallow

clouds are dominant during dry periods in the WGs region. Thus, the larger D_{m} may be due to cumulus congestus during wet spells. The differences in D_{m} during wet and dry spells might occur either at the cloud formation stage and/or during descent of precipitation particles to ground. The microphysical and dynamical processes during descent of precipitation particles are responsible for spatial-temporal variability in D_{m} (Rosenfeld and Ulbrich, 2003). The dominant dynamical processes that affect D_{m} are updrafts/downdrafts, and advection by horizontal winds. To understand the dynamical mechanisms leading to different microphysical processes during wet and dry periods, we have analyzed temperature, specific humidity, horizontal and vertical winds for 2012-2015 monsoon. Figure 9 shows the anomalies in specific humidity ($\mathrm{kg\,kg^{-1}}$, shading), temperature (K, contours), and horizontal winds (vectors) at 850 hPa derived from ERA-Interim dataset. This pressure level is selected, as the temperature anomaly and moisture availability aid the growth of active convection. The daily 0000 UTC ERA-Interim data for ten years (2006-2015) is considered to find anomalies. The seasonal averages are calculated for different atmospheric parameters and the anomalies are estimated as the difference between wet/dry period mean and seasonal mean. Here, positive anomalies in specific humidity (temperature) represent an increase in moisture content (heating), and negative anomaly represents a decrease in specific humidity (cooling). It is observed that the temperature is cooler over the west coast of India (including the study region) in wet spells than dry periods. This figure also shows that the anomalous winds are maritime, and continental during wet and dry spells, respectively. The anomalous winds coming from the oceanic region brings more moisture (positive anomalies in specific humidity) over WGs during wet spells. Whereas, the anomalous winds coming from the continent brings dry (negative anomalies in specific humidity) air during dry spells. The thermal gradient between WGs and surrounding regions and the availability of more moisture favours active convection in the wet spells. Whereas, positive temperature anomalies in the dry spell can lead to evaporation of raindrops, which can subsequently break the drops, thereby leading to lesser diameter drops.

To understand the effect of updrafts/downdrafts on D_{m} variability, omega (vertical motion in pressure coordinate) field is analyzed for the region 17-18° N and 73-74° E. Figure 10 shows the vertical profile of omega during wet and dry spells. Here, negative values of omega represent updrafts and vice-versa. The mean vertical winds are negative in wet spells indicating updrafts. Whereas the mean vertical winds are small and positive indicating downdrafts during dry spells. The updrafts do not allow the smaller drops to fall, which are carried aloft, where they can fall out later. Hence, the smaller drops have enough time to grow by collision-coalescence process, to form mid-size or large-size drops. Therefore, the medium- or large-size drops increase at the expense of smaller drops, which leads to larger D_{m} during wet spells. Whereas the downward flux of raindrops increases due to the downdrafts, which causes smaller drops reaching the surface. The large density of smaller drops decrease D_{m} during dry spells.

The diurnal variation in mean rain rate during wet and dry spells is shown in Figure 11. The mean rain rate is higher during wet periods throughout the day. The relatively lower rain rates are due to higher concentration of smaller drops during dry spells. The diurnal variation in rain rate shows bi-modal distribution during both wet and dry spells. The primary maximum is in afternoon hours and the secondary maximum is during morning hours. The raindrop concentration increases monotonically (refer Figure 5), with an increase in rain rate for all the drop sizes during dry spells. This finding indicates that the increase in rain rate is responsible for rise in both concentration and raindrop size during dry spells. However, in wet periods, the

concentration of smaller drops is constant throughout the day, and the increase in rain rate is due to the rise in concentration and size of mid-size raindrops. This further indicates that the collision and coalescence processes and deposition of water vapour on to the cloud drops are responsible for increased concentration (afternoon and early morning hours) of mid-size raindrops during wet spells. In addition, the raindrop diameter depends on rain rate, which varies between wet and dry spells. The D_{m} distribution during wet and dry spells at different rain rates are shown in Figure 12. The D_{m} is higher in wet spells than dry spells below 10 $\mathrm{mm\,h^{-1}}$. This could be due to the deposition of water vapour and accretion of cloud water on raindrops. This result in larger D_{m} during wet spells compared to dry spells. At higher rain rates (above 20 $\mathrm{mm\,h^{-1}}$), D_{m} distribution remains the same during both spells. This is due to equilibrium of DSD by collision, coalescence, and breakup mechanisms, as described in Hu and Srivastava (1995) and Atlas and Ulbrich (2000). So, it is evident that the dynamical mechanisms underlying the microphysical processes cause the differences in DSD characteristics during wet and dry spells. The distinct DSD features during ISM's wet and dry spells over WGs are summarized in Figure 13.

5.2 Implications of DSD during wet and dry spells: μ-λ relation

The gamma distribution is widely used in microphysical parameterization schemes in the numerical models to describe various DSDs. However, μ is often considered to be constant. Milbrandt and Yau (2005) found that μ plays a vital role in determining sedimentation and microphysical growth rates. In this context, the microphysical properties of clouds and precipitation are sensitive to variations in μ. Several researchers showed that μ varies during the precipitation (Ulbrich, 1983; Ulbrich and Atlas, 1998; Testud et al., 2001; Zhang et al., 2001; Islam et al., 2012). Zhang et al. (2003) proposed an empirical μ-λ relationship using 2DVD data collected in Florida. They examined μ-λ relation with different rain types. These μ-λ relations are useful in reducing the bias in estimating rain parameters from remote sensing measurements (Zhang et al., 2003). Recent studies have demonstrated the variability in μ-λ relation in different types of rain and geographical locations (Chang et al., 2009; Kumar et al., 2011; Wen et al., 2016). Hence, it is necessary to derive different μ-λ relations based on local DSD observations.

An empirical μ-λ relationship is derived for both wet and dry spells. The DSDs with rain rate less than 5 $\mathrm{mm\,h^{-1}}$ are excluded to minimize the sampling errors. In addition, the total drop counts above 1000 are only considered in the analysis, as proposed by Zhang et al. (2003). Figure 14 shows μ-λ relation for wet and dry spells, and the corresponding polynomial least-square fits are shown as solid lines. The fitted μ-λ relations for wet and dry spells are given as follows:

Wet spell $$\lambda = 0.0359\mu^2 + 0.802\mu + 2.22 \tag{10}$$

Dry spell $$\lambda = 0.0138\mu^2 + 1.151\mu + 1.198 \tag{11}$$

The above equations represent that the smaller value of λ (higher rain rates), smaller is the value of μ in both spells. Thus, the DSDs tend to be more concave downwards with an increase in rain rate. This finding suggests a higher fraction of small and mid-size drops and a lower fraction of larger drops, reflecting less evaporation of smaller drops and more drop breakup processes. However, the fitted μ-λ relation exhibits a large difference between wet and dry spells. Comparing Eq. (10) and

(11), one can observe that the coefficient of linear term is smaller in wet spells than that of dry spells. Hence, for a given μ, the dry spells have higher λ compared to the wet spells. Further, D_{m} is higher during wet spells than dry spells for a given rainfall rate due to different microphysical mechanisms discussed above (Figure 12). This leads to higher μ in wet spells than dry spells, which indicates different microphysical mechanisms lead to different μ-λ relations. Hence, it is apparent that a single μ-λ relation cannot reliably represent the observed phenomenon during different monsoon phases.

Further, μ-λ relationships are derived for convective and stratiform rain as:

$$\text{Convective rain} \qquad \lambda = 0.0069\mu^2 + 0.576\mu + 2.42 \tag{12}$$

$$\text{Stratiform rain} \qquad \lambda = 0.0022\mu^2 + 0.933\mu + 1.86 \tag{13}$$

Seela et al. (2018) fitted μ-λ relations for summer and winter rainfall over North Taiwan. Chen et al. (2017) derived an empirical μ-λ relation over Tibetan Plateau. Cao et al. (2008) analyzed μ-λ relations over Oklahoma. Different μ-λ relations are derived for different weather systems over North Taiwan (Chu and Su, 2008). The μ-λ relationship obtained in this work differs from Zhang et al. (2003), Chu and Su (2008), and Seela et al. (2018). The differences in μ-λ relations could be attributed several factors like geographical location, microphysical processes, rain rate, and type of instrument. To explore the plausible effect of rainfall rate, μ-λ relations are compared with the previous studies for rain rates below 5 $\mathrm{mm\,h^{-1}}$ (as in Chu and Su, 2008), and above 5 $\mathrm{mm\,h^{-1}}$ (as in Zhang et al., 2003) (figure not shown). It is observed that μ-λ relations in this work differ from previous studies in both rain rate regions. Further, the slope of μ-λ relationship is higher over WGs than previous studies. This shows that the wet and dry spells have higher μ than previous studies for same λ indicating that the underlying microphysical processes are different over complex orographic region, WGs. Further, D_{m} in the present study is higher than previous studies (e.g., Seela et al., 2018). The different D_{m} distributions lead to different μ values (Ulbrich, 1983). Thus, relatively higher D_{m} values could contribute to higher μ for the same λ values in the present study. Hence, the differences in μ-λ relations with previous studies may be related to different rain microphysics (such as collision-coalescence, breakup, etc.). In addition, Zhang et al. (2003), and Chu and Su (2008) used 2DVD measurements, whereas, JWD data are utilized in this work. The different instruments can have different sensitivities, which can also affect μ-λ relations. The μ-λ relationships derived for the current study are compared with the other orographic precipitations and are provided in Table 5. It is clear that μ-λ relations vary in different types of rainfall and climatic regimes.

6 Conclusions

The raindrop spectra measured by JWD are analyzed to understand the DSD variations during wet and dry spells of ISM over WGs. Observational results indicate that the DSDs are considerably different during wet and dry periods. In addition, the DSD variability is studied with stratiform and convective rain during wet and dry spells. Key findings are listed below:

i. A high concentration of smaller drops is always present in the WGs region, indicating shallow convection dominance.

ii. The DSD over WGs shows distinct diurnal features. The dry spells exhibit a strong diurnal cycle with double-peak during late afternoon and night time in smaller and mid-size drops. Whereas, this diurnal cycle is weak for smaller drops in wet spells.

iii. Small D_m, and large N_w characterize the DSDs over WGs. The N_w shows a bi-modal distribution during dry spells. This bimodality is weak in wet spells. The distribution of λ shows dominance of small drops in dry spells and mid-size drops in wet spells.

iv. The thermal gradient between WGs and surrounding regions, higher availability of water vapour, and strong vertical winds favours the formation of cumulus congestus, which are responsible for the presence of mid-size/larger drops during wet spells.

v. The empirical relation between μ and λ shows a significant difference between wet and dry spells. The different microphysical mechanisms lead to different μ-λ relations.

It is evident from this study that, even though the warm rain is predominant, the dynamical mechanisms underlying the microphysical processes are different, which causes the difference in observed DSD characteristics during wet and dry spells.

Data availability. The disdrometer data are archived at IITM and are available with the corresponding author (skd_ncu@yahoo.com) for research collaboration. GPM and ERA-Interim datasets were respectively downloaded from https://pmm.nasa.gov/data-access/downloads/gpm. and https://www.ecmwf.int.

Author contributions. UVMK and SKD designed, analyzed, and prepared the manuscript. SKD, UVMK, and UB proposed the methodology. GSE, SMD, and GP contributed with discussion to the manuscript.

Competing interests. The authors declare that there is no conflict of interest.

Acknowledgements. The authors are thankful to the Director, IITM, for his support. The authors would like to acknowledge the technical/administrative staff of the High Altitude Cloud Physics Laboratory (HAPCL), Mahabaleshwar, for maintaining disdrometer. The authors acknowledge the India Meteorological Department (IMD) for the provision of rainfall dataset. The authors also acknowledge the JAXA, JAPAN, and NASA, USA, for providing GPM data (https://pmm.nasa.gov/data-access/downloads/gpm). The authors would like to acknowledge the European Centre for Medium-Range Weather Forecasts (ECMWF) for providing ERA-Interim dataset. The manuscript benefitted from comments and suggestions provided by the Editor and the anonymous reviewers

References

Atlas, D. and Ulbrich, C. W.: An observationally based conceptual model of warm oceanic convective rain in the tropics, Journal of Applied Meteorology, 39, 2165–2181, 2000.

Atlas, D., Ulbrich, C. W., Marks Jr, F. D., Amitai, E., and Williams, C. R.: Systematic variation of drop size and radar-rainfall relations, Journal of Geophysical Research: Atmospheres, 104, 6155–6169, 1999.

Bringi, V., Chandrasekar, V., Hubbert, J., Gorgucci, E., Randeu, W., and Schoenhuber, M.: Raindrop size distribution in different climatic regimes from disdrometer and dual-polarized radar analysis, Journal of the atmospheric sciences, 60, 354–365, 2003.

Bringi, V. N. and Chandrasekar, V.: Polarimetric Doppler weather radar: principles and applications, Cambridge university press, 2001.

Cao, Q. and Zhang, G.: Errors in estimating raindrop size distribution parameters employing disdrometer and simulated raindrop spectra, Journal of Applied Meteorology and Climatology, 48, 406–425, 2009.

Cao, Q., Zhang, G., Brandes, E., Schuur, T., Ryzhkov, A., and Ikeda, K.: Analysis of video disdrometer and polarimetric radar data to characterize rain microphysics in Oklahoma, Journal of Applied Meteorology and Climatology, 47, 2238–2255, 2008.

Chang, W.-Y., Wang, T.-C. C., and Lin, P.-L.: Characteristics of the raindrop size distribution and drop shape relation in typhoon systems in the western Pacific from the 2D video disdrometer and NCU C-band polarimetric radar, Journal of Atmospheric and Oceanic Technology, 26, 1973–1993, 2009.

Chen, B., Hu, Z., Liu, L., and Zhang, G.: Raindrop Size Distribution Measurements at 4,500 m on the Tibetan Plateau During TIPEX-III, Journal of Geophysical Research: Atmospheres, 122, 11–092, 2017.

Chu, Y.-H. and Su, C.-L.: An investigation of the slope–shape relation for gamma raindrop size distribution, Journal of Applied Meteorology and Climatology, 47, 2531–2544, 2008.

Das, S. K., Uma, K., Konwar, M., Raj, P. E., Deshpande, S., and Kalapureddy, M.: CloudSat–CALIPSO characterizations of cloud during the active and the break periods of Indian summer monsoon, Journal of Atmospheric and Solar-Terrestrial Physics, 97, 106–114, 2013.

Das, S. K., Konwar, M., Chakravarty, K., and Deshpande, S. M.: Raindrop size distribution of different cloud types over the Western Ghats using simultaneous measurements from Micro-Rain Radar and disdrometer, Atmospheric Research, 186, 72–82, 2017.

Das, S. K., Simon, S., Kolte, Y. K., Krishna, U. M., Deshpande, S. M., and Hazra, A.: Investigation of raindrops fall velocity during different monsoon seasons over the Western Ghats, India, Earth and Space Science, 7, e2019EA000 956, 2020.

Dee, D. P., Uppala, S. M., Simmons, A., Berrisford, P., Poli, P., Kobayashi, S., Andrae, U., Balmaseda, M., Balsamo, G., Bauer, d. P., et al.: The ERA-Interim reanalysis: Configuration and performance of the data assimilation system, Quarterly Journal of the royal meteorological society, 137, 553–597, 2011.

Deshpande, N. and Goswami, B.: Modulation of the diurnal cycle of rainfall over India by intraseasonal variations of Indian summer monsoon, International journal of climatology, 34, 793–807, 2014.

Dolan, B., Fuchs, B., Rutledge, S., Barnes, E., and Thompson, E.: Primary modes of global drop size distributions, Journal of the Atmospheric Sciences, 75, 1453–1476, 2018.

Dolman, B. K., May, P. T., M, R. I., and A, V. R.: Profiler retrieved DSD evolution in the tropics and mid-latitudes, in: 35th International Conference on Radar Meteorology, 2011.

Farr, T. G., Rosen, P. A., Caro, E., Crippen, R., Duren, R., Hensley, S., Kobrick, M., Paller, M., Rodriguez, E., Roth, L., et al.: The shuttle radar topography mission, Reviews of geophysics, 45, 2007.

Friedrich, K., Kalina, E. A., Masters, F. J., and Lopez, C. R.: Drop-size distributions in thunderstorms measured by optical disdrometers during VORTEX2, Monthly weather review, 141, 1182–1203, 2013.

Gadgil, S. and Joseph, P.: On breaks of the Indian monsoon, Journal of Earth System Science, 112, 529–558, 2003.

Gao, W., Sui, C.-H., Chen Wang, T.-C., and Chang, W.-Y.: An evaluation and improvement of microphysical parameterization from a two-moment cloud microphysics scheme and the Southwest Monsoon Experiment (SoWMEX)/Terrain-influenced Monsoon Rainfall Experiment (TiMREX) observations, Journal of Geophysical Research: Atmospheres, 116, 2011.

Giangrande, S. E., Feng, Z., Jensen, M. P., Comstock, J. M., Johnson, K. L., Toto, T., Wang, M., Burleyson, C., Bharadwaj, N., Fan, M., et al.: Cloud characteristics, thermodynamic controls and radiative impacts during the Observations and Modeling of the Green Ocean Amazon (GoAmazon2014/5) experiment, Atmospheric Chemistry and Physics, 17, 14 519, 2017.

Goswami, B. N. and Mohan, R. A.: Intraseasonal oscillations and interannual variability of the Indian summer monsoon, Journal of Climate, 14, 1180–1198, 2001.

Harikumar, R.: Orographic effect on tropical rain physics in the Asian monsoon region, Atmospheric Science Letters, 17, 556–563, 2016.

Harikumar, R., Sampath, S., and Kumar, V. S.: An empirical model for the variation of rain drop size distribution with rain rate at a few locations in southern India, Advances in Space Research, 43, 837–844, 2009.

Harikumar, R., Sampath, S., and Sasi Kumar, V.: Altitudinal and temporal evolution of raindrop size distribution observed over a tropical station using a K-band radar, International journal of remote sensing, 33, 3286–3300, 2012.

Houze, R. A.: Orographic effects on precipitating clouds, Reviews of Geophysics, 50, 2012.

Hoyos, C. D. and Webster, P. J.: The role of intraseasonal variability in the nature of Asian monsoon precipitation, Journal of Climate, 20, 4402–4424, 2007.

Hu, Z. and Srivastava, R.: Evolution of raindrop size distribution by coalescence, breakup, and evaporation: Theory and observations, Journal of the atmospheric sciences, 52, 1761–1783, 1995.

Huffman, G. J., Bolvin, D. T., Braithwaite, D., Hsu, K., Joyce, R., Xie, P., and Yoo, S.-H.: NASA global precipitation measurement (GPM) integrated multi-satellite retrievals for GPM (IMERG), Algorithm Theoretical Basis Document (ATBD) Version, 4, 26, 2015.

Islam, T., Rico-Ramirez, M. A., Thurai, M., and Han, D.: Characteristics of raindrop spectra as normalized gamma distribution from a Joss–Waldvogel disdrometer, Atmospheric Research, 108, 57–73, 2012.

Joss, J. and Gori, E. G.: The parametrization of raindrop size distributions., Rivista Italiana di Geofisica, 3, 273–283, 1976.

Joss, J. and Waldvogel, A.: Raindrop size distribution and sampling size errors, Journal of the Atmospheric Sciences, 26, 566–569, 1969.

Konwar, M., Das, S., Deshpande, S., Chakravarty, K., and Goswami, B.: Microphysics of clouds and rain over the Western Ghat, Journal of Geophysical Research: Atmospheres, 119, 6140–6159, 2014.

Krishna, U. M., Reddy, K. K., Seela, B. K., Shirooka, R., Lin, P.-L., and Pan, C.-J.: Raindrop size distribution of easterly and westerly monsoon precipitation observed over Palau islands in the Western Pacific Ocean, Atmospheric Research, 174, 41–51, 2016.

Kulkarni, A., Kripalani, R., Sabade, S., and Rajeevan, M.: Role of intra-seasonal oscillations in modulating Indian summer monsoon rainfall, Climate dynamics, 36, 1005–1021, 2011.

Kumar, L. S., Lee, Y. H., and Ong, J. T.: Two-parameter gamma drop size distribution models for Singapore, IEEE Transactions on Geoscience and Remote Sensing, 49, 3371–3380, 2011.

Kumar, S., Hazra, A., and Goswami, B.: Role of interaction between dynamics, thermodynamics and cloud microphysics on summer monsoon precipitating clouds over the Myanmar Coast and the Western Ghats, Climate dynamics, 43, 911–924, 2014.

Kumar, V. S., Sampath, S., Vinayak, P., and Harikumar, R.: Rainfall intensity characteristics at coastal and high altitude stations in Kerala, Journal of earth system science, 116, 451–463, 2007.

Lavanya, S., Kirankumar, N., Aneesh, S., Subrahmanyam, K., and Sijikumar, S.: Seasonal variation of raindrop size distribution over a coastal station Thumba: A quantitative analysis, Atmospheric research, 229, 86–99, 2019.

Liao, L., Meneghini, R., Iguchi, T., and Detwiler, A.: Validation of snow parameters as derived from dual-wavelength airborne radar, in: 31st International Conference on Radar Meteorology, 2003.

Liao, L., Meneghini, R., and Tokay, A.: Uncertainties of GPM DPR rain estimates caused by DSD parameterizations, Journal of Applied Meteorology and Climatology, 53, 2524–2537, 2014.

Machado, L. A., Calheiros, A. J., Biscaro, T., Giangrande, S., Silva Dias, M. A., Cecchini, M. A., Albrecht, R., Andreae, M. O., Araujo, W. F., Artaxo, P., et al.: Overview: Precipitation characteristics and sensitivities to environmental conditions during GoAmazon2014/5 and ACRIDICON-CHUVA, Atmospheric Chemistry and Physics (Online), 18, 2018.

Maheskumar, R., Narkhedkar, S., Morwal, S., Padmakumari, B., Kothawale, D., Joshi, R., Deshpande, C., Bhalwankar, R., and Kulkarni, J.: Mechanism of high rainfall over the Indian west coast region during the monsoon season, Climate dynamics, 43, 1513–1529, 2014.

Mardiana, R., Iguchi, T., and Takahashi, N.: A dual-frequency rain profiling method without the use of a surface reference technique, IEEE transactions on geoscience and remote sensing, 42, 2214–2225, 2004.

Meneghini, R., Kumagai, H., Wang, J. R., Iguchi, T., and Kozu, T.: Microphysical retrievals over stratiform rain using measurements from an airborne dual-wavelength radar-radiometer, IEEE transactions on geoscience and remote sensing, 35, 487–506, 1997.

Milbrandt, J. and Yau, M.: A multimoment bulk microphysics parameterization. Part I: Analysis of the role of the spectral shape parameter, Journal of the atmospheric sciences, 62, 3051–3064, 2005.

Munchak, S. J., Kummerow, C. D., and Elsaesser, G.: Relationships between the raindrop size distribution and properties of the environment and clouds inferred from TRMM, Journal of climate, 25, 2963–2978, 2012.

Murali Krishna, U., Das, S. K., Deshpande, S. M., Doiphode, S., and Pandithurai, G.: The assessment of Global Precipitation Measurement estimates over the Indian subcontinent, Earth and Space Science, 4, 540–553, 2017.

Nair, H. R.: Discernment of near-oceanic precipitating clouds into convective or stratiform based on Z–R model over an Asian monsoon tropical site, Meteorology and Atmospheric Physics, pp. 1–14, 2019.

Narayana Rao, T., Radhakrishna, B., Nakamura, K., and Prabhakara Rao, N.: Differences in raindrop size distribution from southwest monsoon to northeast monsoon at Gadanki, Quarterly Journal of the Royal Meteorological Society: A journal of the atmospheric sciences, applied meteorology and physical oceanography, 135, 1630–1637, 2009.

Pai, D., Sridhar, L., Rajeevan, M., Sreejith, O., Satbhai, N., and Mukhopadhyay, B.: Development of a new high spatial resolution (0.25×0.25) long period (1901–2010) daily gridded rainfall data set over India and its comparison with existing data sets over the region, Mausam, 65, 1–18, 2014.

Radhakrishna, B., Satheesh, S., Narayana Rao, T., Saikranthi, K., and Sunilkumar, K.: Assessment of DSDs of GPM-DPR with ground-based disdrometer at seasonal scale over Gadanki, India, Journal of Geophysical Research: Atmospheres, 121, 11–792, 2016.

Rajeevan, M., Bhate, J., Kale, J., and Lal, B.: High resolution daily gridded rainfall data for the Indian region: Analysis of break and active, Current Science, 91, 296–306, 2006.

Rajeevan, M., Gadgil, S., and Bhate, J.: Active and break spells of the Indian summer monsoon, Journal of earth system science, 119, 229–247, 2010.

Rajeevan, M., Rohini, P., Kumar, K. N., Srinivasan, J., and Unnikrishnan, C.: A study of vertical cloud structure of the Indian summer monsoon using CloudSat data, Climate dynamics, 40, 637–650, 2013.

Rajopadhyaya, D. K., May, P. T., Cifelli, R. C., Avery, S. K., Willams, C. R., Ecklund, W. L., and Gage, K. S.: The effect of vertical air motions on rain rates and median volume diameter determined from combined UHF and VHF wind profiler measurements and comparisons with rain gauge measurements, Journal of Atmospheric and Oceanic Technology, 15, 1306–1319, 1998.

Ramamurthy, K.: Monsoon of India: Some aspects of the "break" in the Indian southwest monsoon during July and August, Tech. rep., India Meteorological Department, 1969.

Rao, T. N., Saikranthi, K., Radhakrishna, B., and Bhaskara Rao, S. V.: Differences in the climatological characteristics of precipitation between active and break spells of the Indian summer monsoon, Journal of Climate, 29, 7797–7814, 2016.

Reddy, K. K. and Kozu, T.: Measurements of raindrop size distribution over Gadanki during south-west and north-east monsoon, 2003.

Romatschke, U. and Houze, R. A.: Characteristics of precipitating convective systems in the South Asian monsoon, Journal of Hydrometeorology, 12, 3–26, 2011.

Rosenfeld, D. and Ulbrich, C. W.: Cloud microphysical properties, processes, and rainfall estimation opportunities, in: Radar and Atmospheric Science: A Collection of Essays in Honor of David Atlas, pp. 237–258, Springer, 2003.

Ryzhkov, A. V., Giangrande, S. E., and Schuur, T. J.: Rainfall estimation with a polarimetric prototype of WSR-88D, Journal of Applied Meteorology, 44, 502–515, 2005.

Satyanarayana Mohan, T. and Narayana Rao, T.: Variability of the thermal structure of the atmosphere during wet and dry spells over southeast India, Quarterly Journal of the Royal Meteorological Society, 138, 1839–1851, 2012.

Seela, B. K., Janapati, J., Lin, P.-L., Wang, P. K., and Lee, M.-T.: Raindrop size distribution characteristics of summer and winter season rainfall over north Taiwan, Journal of Geophysical Research: Atmospheres, 123, 11–602, 2018.

Seto, S., Iguchi, T., and Oki, T.: The Basic Performance of a Precipitation Retrieval Algorithm for the Global Precipitation Measurement Mission's Single/Dual-Frequency Radar Measurements, IEEE Transactions on Geoscience and Remote Sensing, 51, 5239–5251, https://doi.org/10.1109/TGRS.2012.2231686, 2013.

Shige, S., Nakano, Y., and Yamamoto, M. K.: Role of orography, diurnal cycle, and intraseasonal oscillation in summer monsoon rainfall over the Western Ghats and Myanmar Coast, Journal of Climate, 30, 9365–9381, 2017.

Sumesh, R., Resmi, E., Unnikrishnan, C., Jash, D., Sreekanth, T., Resmi, M. M., Rajeevan, K., Nita, S., and Ramachandran, K.: Microphysical aspects of tropical rainfall during Bright Band events at mid and high-altitude regions over Southern Western Ghats, India, Atmospheric Research, 227, 178–197, 2019.

Testud, J., Oury, S., Black, R. A., Amayenc, P., and Dou, X.: The concept of "normalized" distribution to describe raindrop spectra: A tool for cloud physics and cloud remote sensing, Journal of Applied Meteorology, 40, 1118–1140, 2001.

Thompson, E. J., Rutledge, S. A., Dolan, B., and Thurai, M.: Drop size distributions and radar observations of convective and stratiform rain over the equatorial Indian and west Pacific Oceans, Journal of the Atmospheric Sciences, 72, 4091–4125, 2015.

Tokay, A., Kruger, A., and Krajewski, W. F.: Comparison of drop size distribution measurements by impact and optical disdrometers, Journal of Applied Meteorology, 40, 2083–2097, 2001.

Tokay, A., Wolff, R., Bashor, P., and Dursun, O.: On the measurement errors of the Joss–Waldvogel disdrometer, in: 31st International Conference on Radar Meteorology, 2003.

Tokay, A., Bashor, P. G., and Wolff, K. R.: Error characteristics of rainfall measurements by collocated Joss–Waldvogel disdrometers, Journal of atmospheric and oceanic technology, 22, 513–527, 2005.

Ulbrich, C. W.: Natural variations in the analytical form of the raindrop size distribution, Journal of climate and applied meteorology, 22, 1764–1775, 1983.

Ulbrich, C. W. and Atlas, D.: Assessment of the contribution of differential polarization to improved rainfall measurements, Radio Science, 19, 49–57, 1984.

Ulbrich, C. W. and Atlas, D.: Rainfall microphysics and radar properties: Analysis methods for drop size spectra, Journal of Applied Meteorology, 37, 912–923, 1998.

Uma, K., Kumar, K. K., Shankar Das, S., Rao, T., and Satyanarayana, T.: On the vertical distribution of mean vertical velocities in the convective regions during the wet and dry spells of the monsoon over Gadanki, Monthly weather review, 140, 398–410, 2012.

Utsav, B., Deshpande, S. M., Das, S. K., and Pandithurai, G.: Statistical characteristics of convective clouds over the Western Ghats derived from weather radar observations, Journal of Geophysical Research: Atmospheres, 122, 10–050, 2017.

Utsav, B., Deshpande, S. M., Das, S. K., Pandithurai, G., and Niyogi, D.: Observed vertical structure of convection during dry and wet summer monsoon epochs over the Western Ghats, Journal of Geophysical Research: Atmospheres, 124, 1352–1369, 2019.

Varikoden, H., Revadekar, J., Kuttippurath, J., and Babu, C.: Contrasting trends in southwest monsoon rainfall over the Western Ghats region of India, Climate Dynamics, 52, 4557–4566, 2019.

Viltard, N., Kummerow, C., Olson, W. S., and Hong, Y.: Combined use of the radar and radiometer of TRMM to estimate the influence of drop size distribution on rain retrievals, Journal of Applied Meteorology, 39, 2103–2114, 2000.

Wen, L., Zhao, K., Zhang, G., Xue, M., Zhou, B., Liu, S., and Chen, X.: Statistical characteristics of raindrop size distributions observed in East China during the Asian summer monsoon season using 2-D video disdrometer and Micro Rain Radar data, Journal of Geophysical Research: Atmospheres, 121, 2265–2282, 2016.

White, A. B., Neiman, P. J., Ralph, F. M., Kingsmill, D. E., and Persson, P. O. G.: Coastal orographic rainfall processes observed by radar during the California Land-Falling Jets Experiment, Journal of Hydrometeorology, 4, 264–282, 2003.

Zagrodnik, J. P., McMurdie, L. A., Houze Jr, R. A., and Tanelli, S.: Vertical Structure and Microphysical Characteristics of Frontal Systems Passing over a Three-Dimensional Coastal Mountain Range, Journal of the Atmospheric Sciences, 76, 1521–1546, 2019.

Zhang, G., Vivekanandan, J., and Brandes, E.: A method for estimating rain rate and drop size distribution from polarimetric radar measurements, IEEE Transactions on Geoscience and Remote Sensing, 39, 830–841, 2001.

Zhang, G., Vivekanandan, J., Brandes, E. A., Meneghini, R., and Kozu, T.: The shape–slope relation in observed gamma raindrop size distributions: Statistical error or useful information?, Journal of Atmospheric and Oceanic Technology, 20, 1106–1119, 2003.

Zhang, G., Xue, M., Cao, Q., and Dawson, D.: Diagnosing the intercept parameter for exponential raindrop size distribution based on video disdrometer observations: Model development, Journal of applied meteorology and climatology, 47, 2983–2992, 2008.

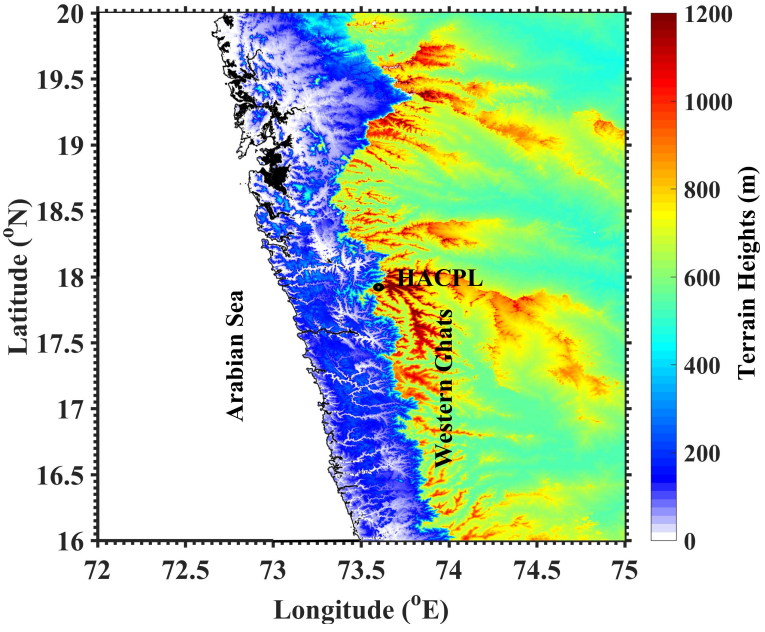

01.jpg

Figure 1. Topographical map of India's Western Ghats generated by using Shuttle Radar Topography Mission (SRTM) data (Farr et al., 2007). Location of the disdrometer installed at HACPL is shown with a black circle.

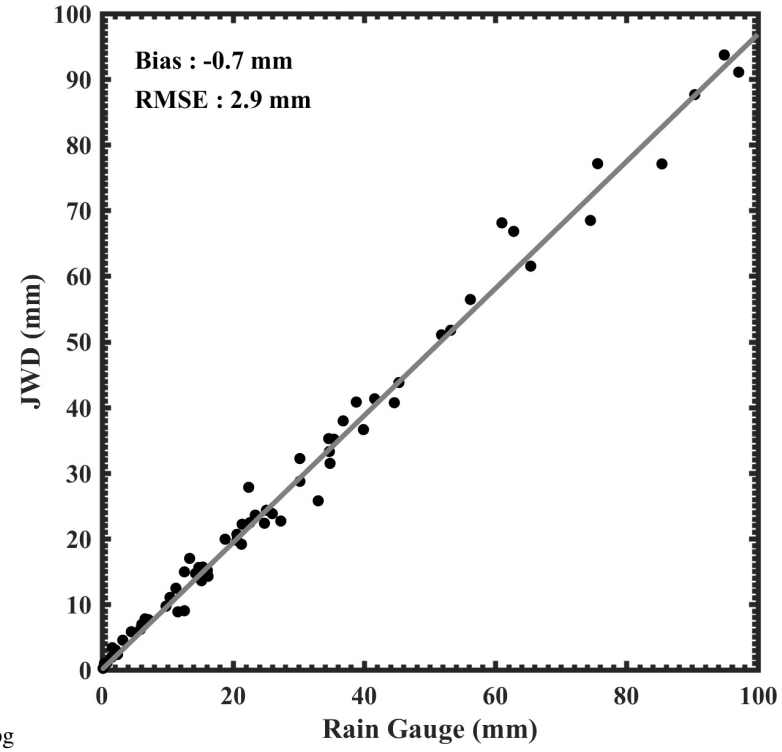

02.jpg

Figure 2. Scatter plot of daily accumulated rainfall between rain gauge and JWD. The solid grey line indicates the linear regression.

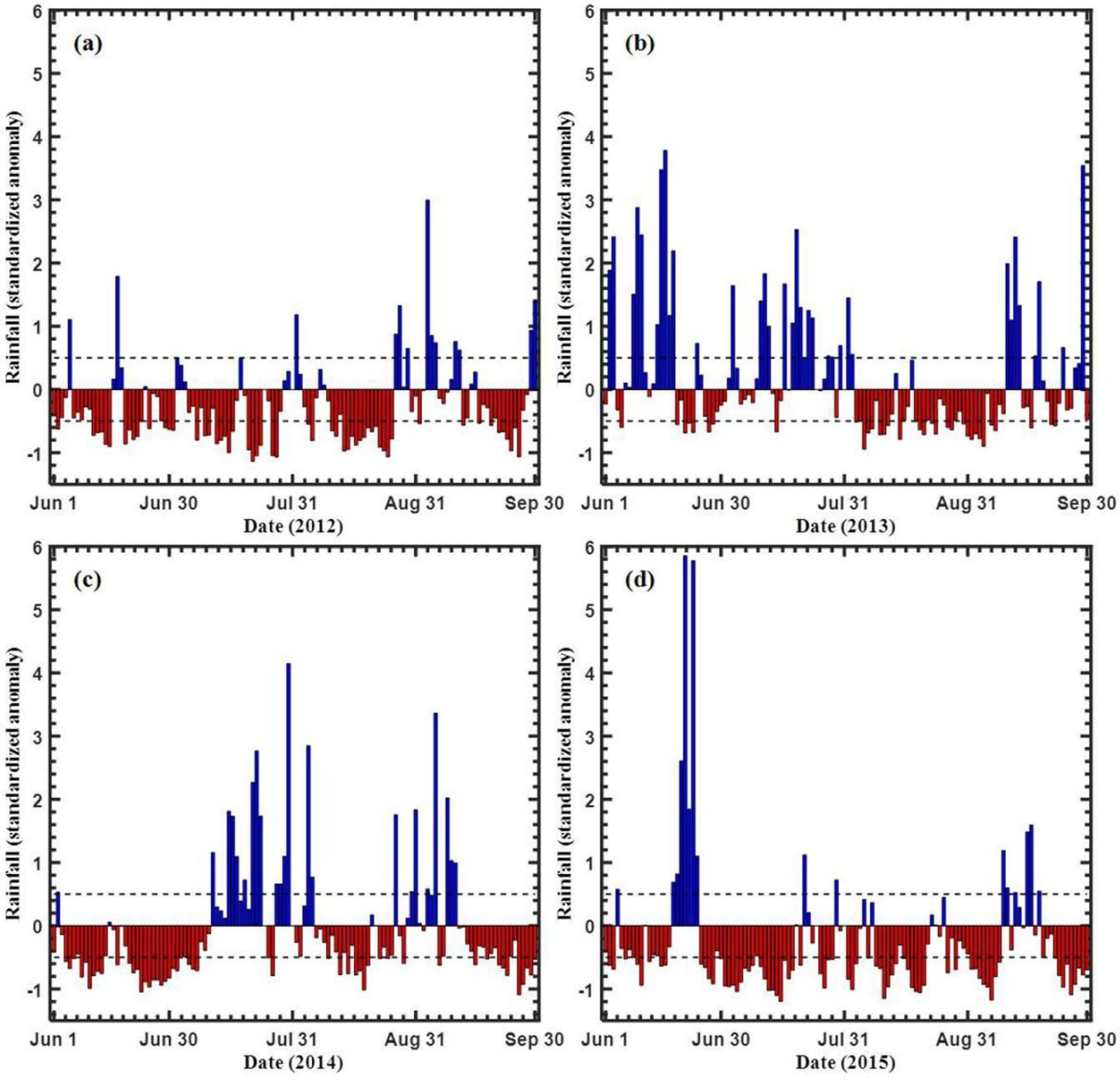

03.jpg

Figure 3. The standardized rainfall anomaly for the year (a) 2012, (b) 2013, (c) 2014, and (d) 2015 during June-September. The dashed line marked for 0.5 (+ve Y-axis) and -0.5 (-ve Y-axis) rainfall anomaly.

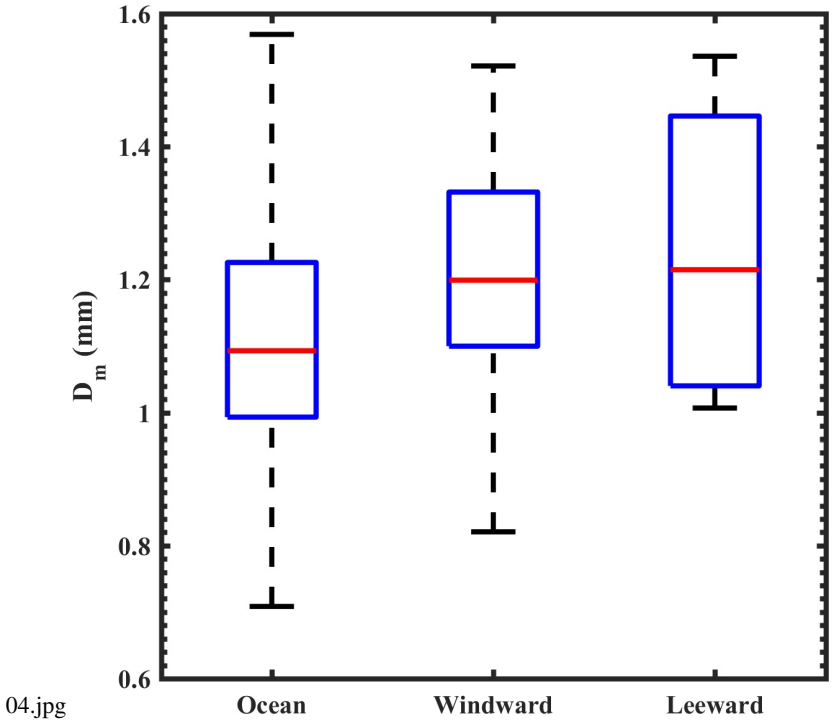

04.jpg

Figure 4. Box and whisker plot of D_m distributions over the ocean, windward (HACPL), and leeward side of the mountain from GPM measurements. Box represents the data between first and third quartiles, and the whiskers show the data from 12.5 and 87.5 percentiles. The horizontal line within the box represents the median value of distribution.

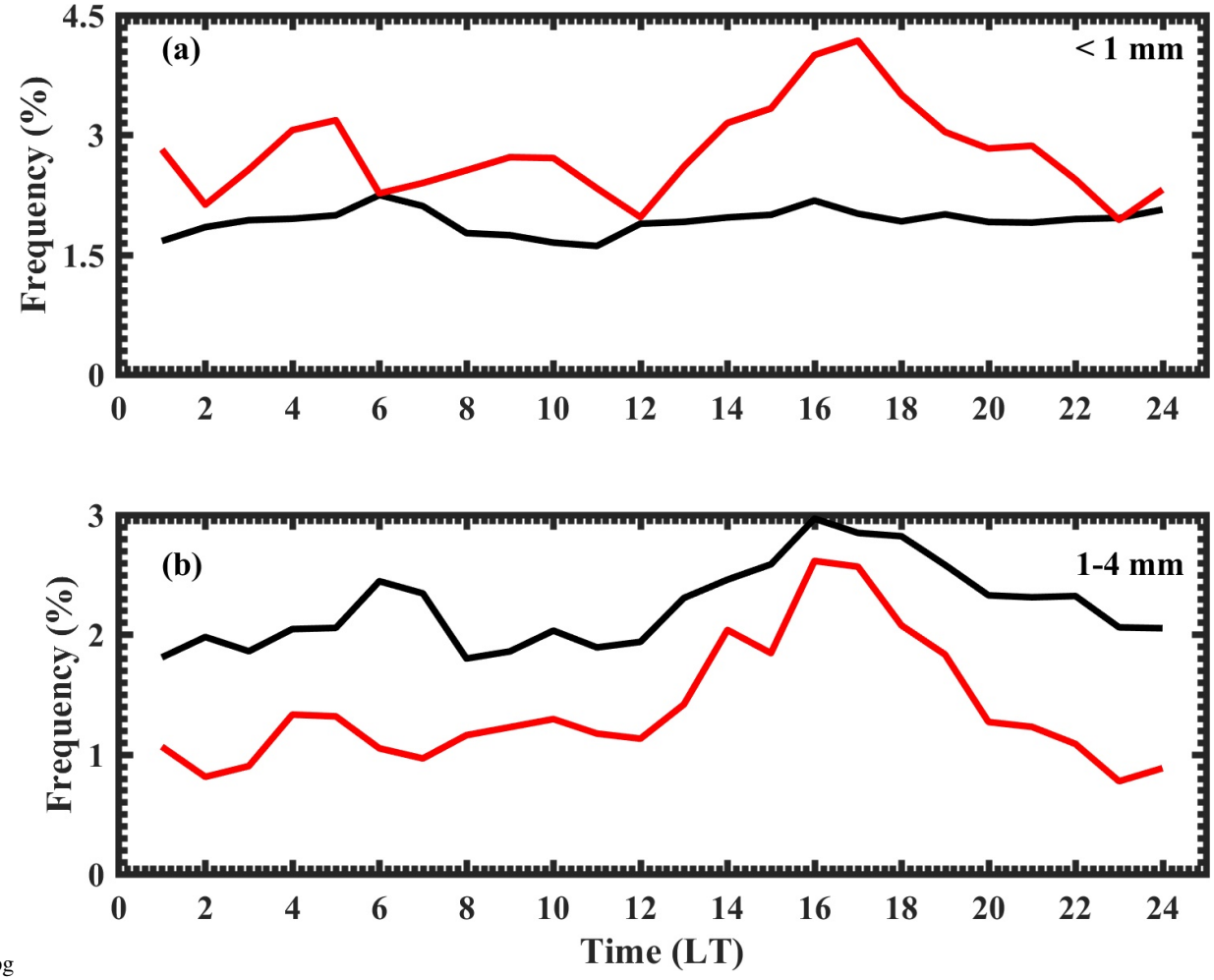

05.jpg

Figure 5. Diurnal variation in raindrop concentration during wet and dry spells for (a) smaller drops (< 1 mm) and (b) mid-size drops (1-4 mm). The concentration of raindrops within each hour is normalized with the total concentration of raindrops in the respective spells (wet or dry). The black line represents wet spells, and the red line represents dry spells.

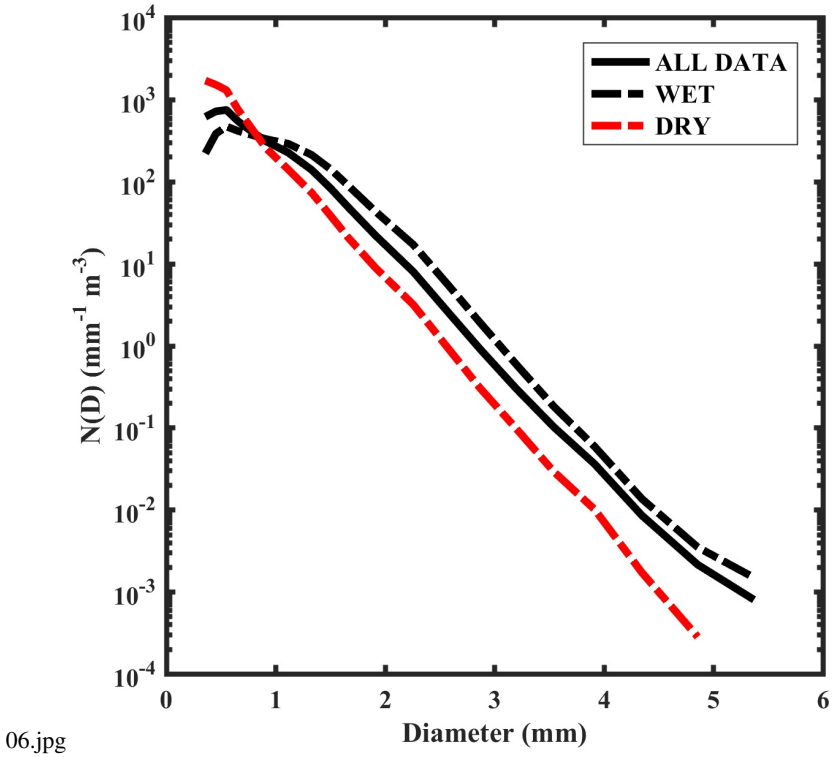

06.jpg

Figure 6. Average DSDs during wet and dry spells

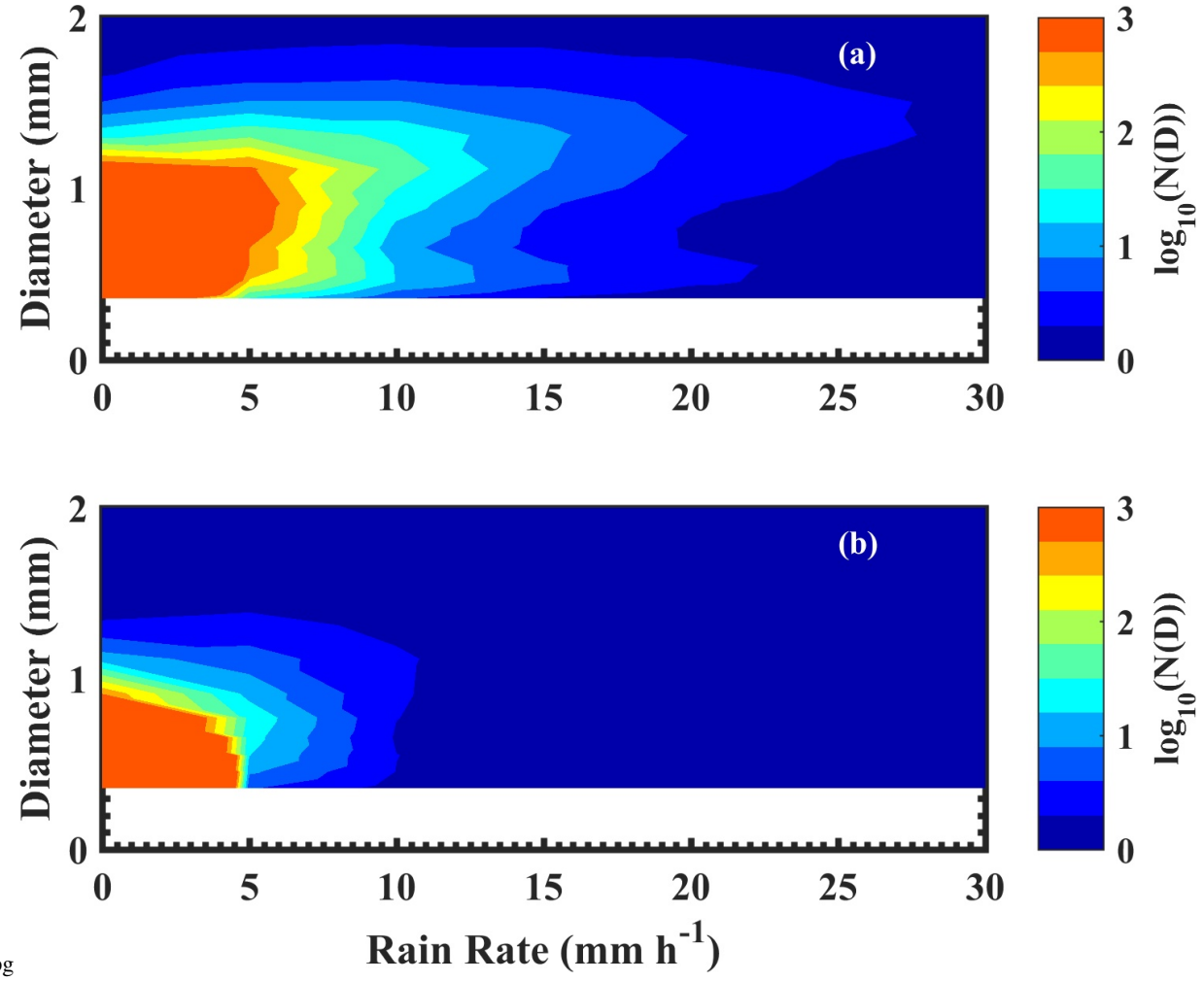

07.jpg

Figure 7. The variation in $N(D)$ as a function of D at different rain rates for (a) wet and (b) dry spells.

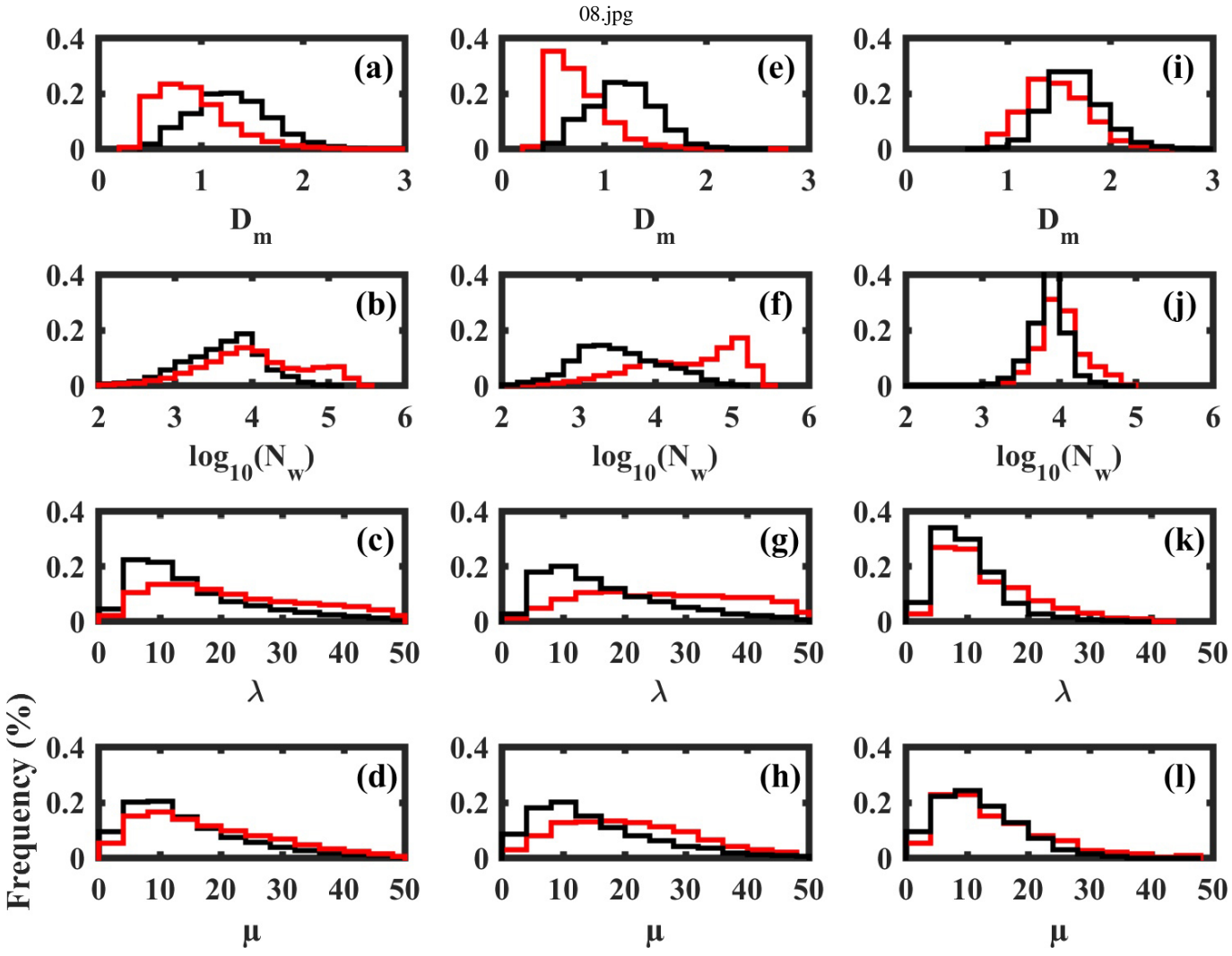

Figure 8. Histograms of (a) D_m, (b) $\log_{10}(N_w)$, (c) λ, and (d) μ for wet and dry spells. (e)-(h) same as (a)-(d), but for stratiform rain. (i)-(l) same as (a)-(d), but for convective rain. Here, the black and red line represents wet and dry spells respectively.

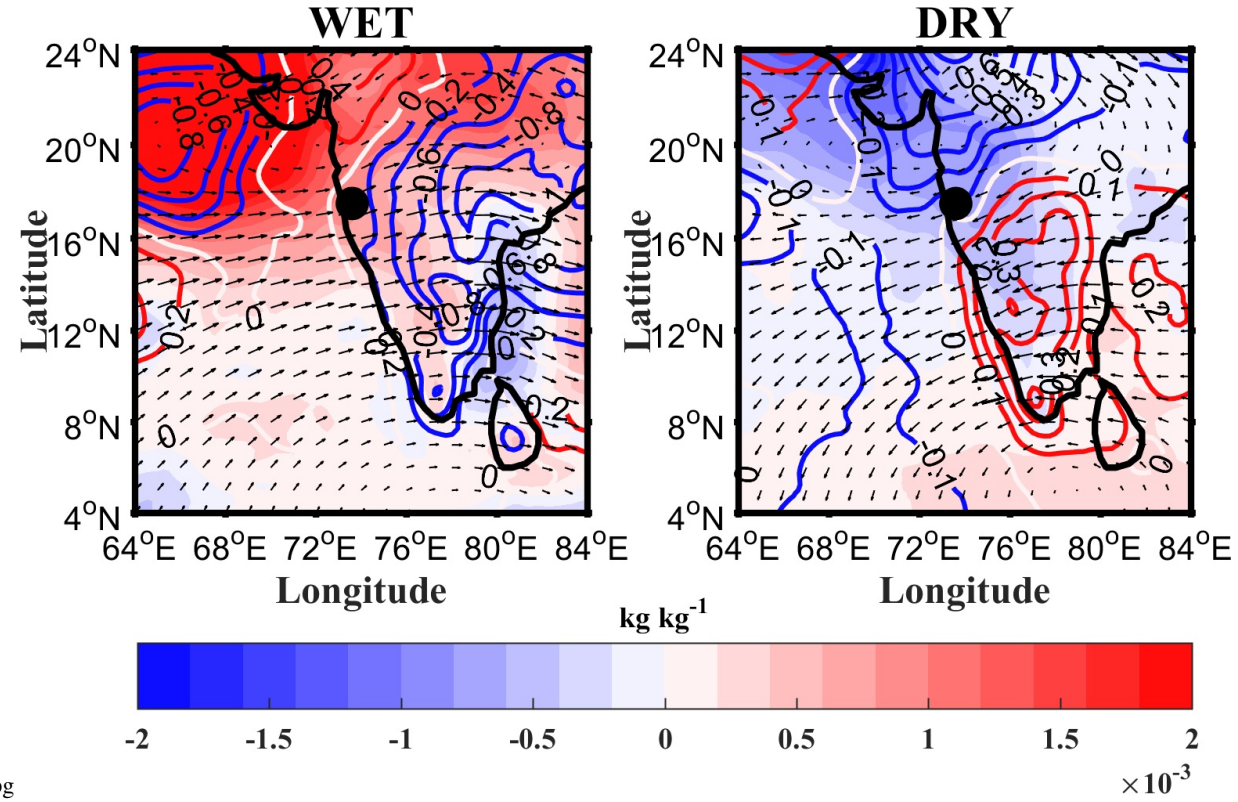

Figure 9. Spatial distribution of anomalies in specific humidity (kg kg^{-1}, shading), temperature (K, contours), and horizontal winds (vectors) at 850 hPa during wet and dry spells of monsoon for 2012-2015. Here, positive anomalies in specific humidity (temperature) represents an increase in moisture content (heating), and negative anomaly represents a decrease in moisture (cooling). The black dot represents the observational site.

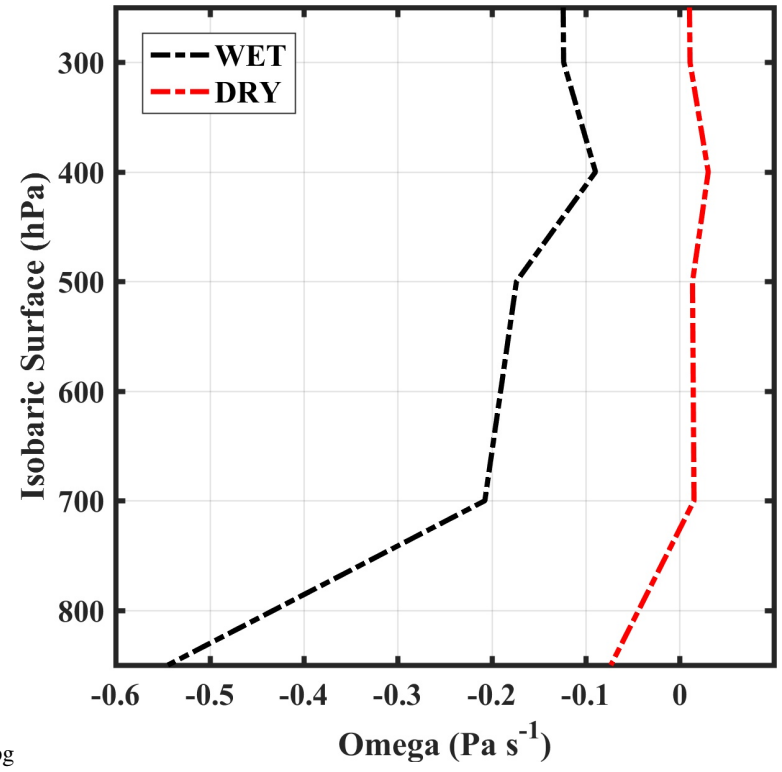

10.jpg

Figure 10. The mean profile of omega for wet and dry spells.

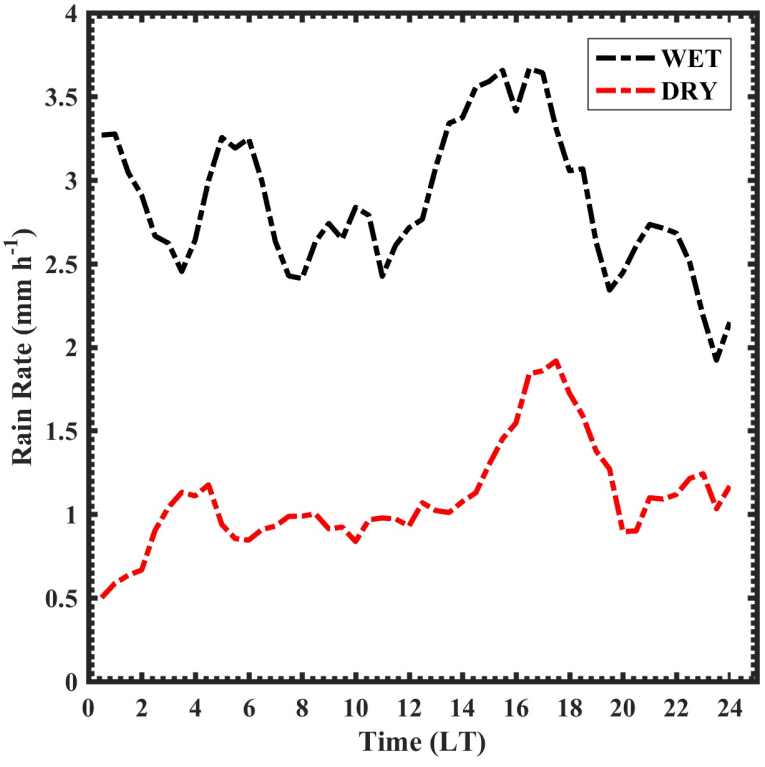

11.jpg

Figure 11. Diurnal variation of mean rain rate ($\mathrm{mm\,h^{-1}}$) for wet and dry spells.

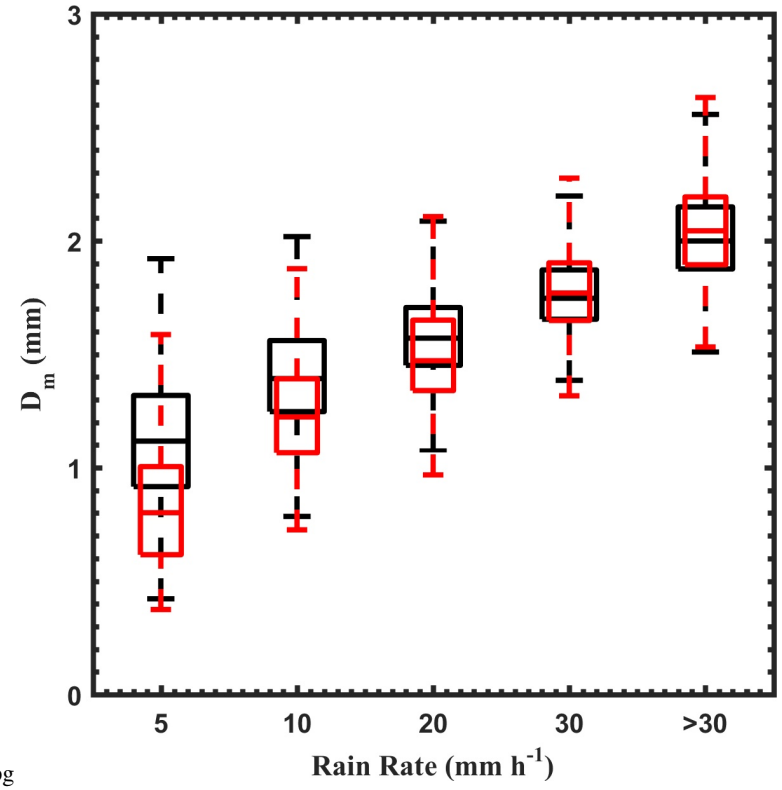

12.jpg

Figure 12. Distribution of D_m at different rain rates for wet and dry spells. The horizontal line within the box represents the median value. The boxes represent data between first and third quartiles, and the whiskers show data from 12.5 to 87.5 percentiles. The black colour represents wet spells, and the red colour represents dry spells.

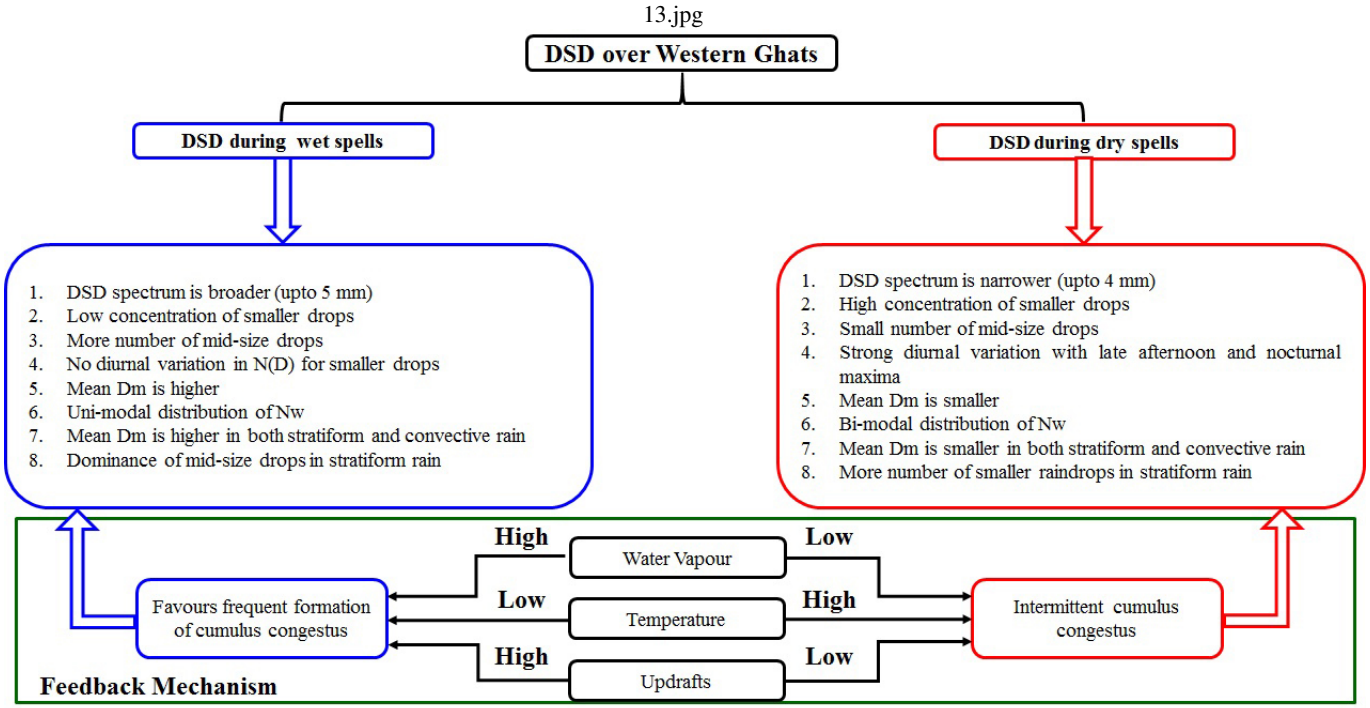

Figure 13. Summary of DSD characteristics for wet and dry spells in the WGs region.

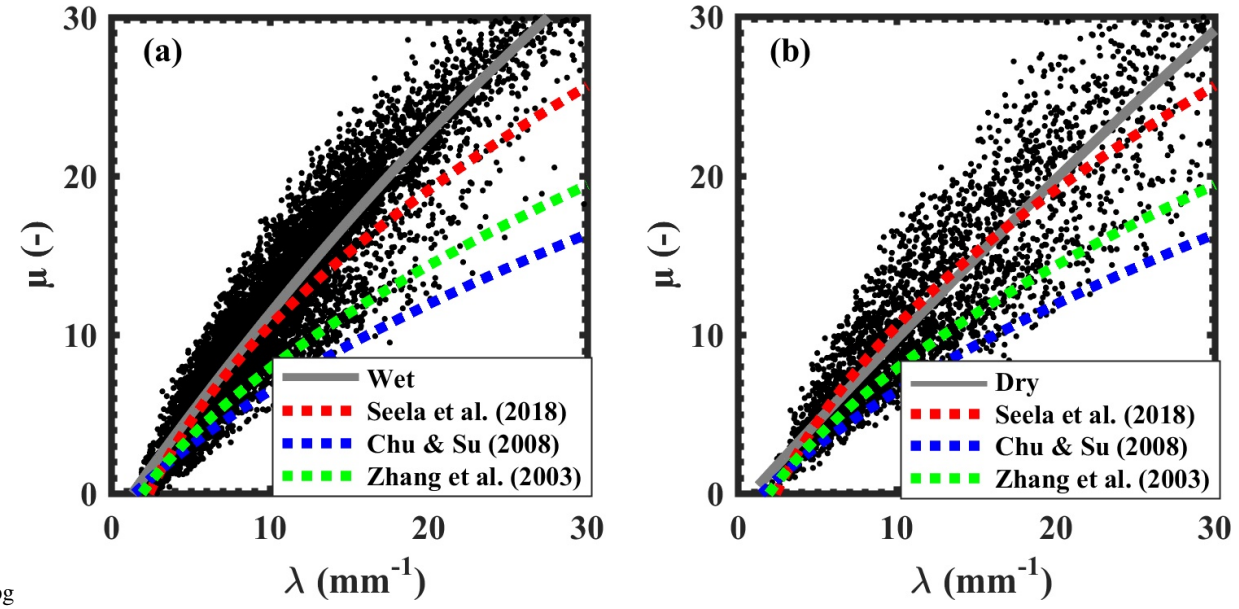

14.jpg

Figure 14. Scatter plots of μ-λ values obtained from gamma DSD for (a) wet and (b) dry spells. The solid line indicates the least square polynomial fit for μ-λ relation.

Table 1. Total number of wet and dry days during monsoon (June-September) of 2012 – 2015.

Months	Wet (No. of. Days)	Dry (No. of. Days)
June	15	40
July	16	38
August	0	46
September	10	35

Table 2. Mean, standard deviation, and skewness of the DSD parameters in wet and dry spells.

	Wet			**Dry**		
	Mean	**Standard deviation**	**Skewness**	**Mean**	**Standard deviation**	**Skewness**
$\boldsymbol{D_m}$	1.30	0.38	0.56	0.92	0.37	1.41
$\mathbf{log_{10}}(\boldsymbol{N_w})$	3.62	0.51	-0.52	4.46	0.68	-0.23
λ	15.42	10.25	1.17	22.01	12.43	0.48
μ	14.40	9.94	1.09	17.80	11.02	0.70
R	6.62	9.75	3.19	2.79	5.02	4.59

Table 3. Mean, standard deviation, and skewness of the DSD parameters in stratiform rain for wet and dry spells.

	Wet			**Dry**		
	Mean	**Standard deviation**	**Skewness**	**Mean**	**Standard deviation**	**Skewness**
$\boldsymbol{D_m}$	1.18	0.31	0.14	0.75	0.265	1.28
$\boldsymbol{\log_{10}(N_w)}$	3.52	0.56	0.19	4.39	0.68	-0.69
λ	17.08	10.56	0.97	26.77	12.48	0.61
μ	15.12	10.17	1.02	20.81	10.76	0.40

Table 4. Mean, standard deviation, and skewness of the DSD parameters in convective rain for wet and dry spells.

	Wet			Dry		
	Mean	**Standard deviation**	**Skewness**	**Mean**	**Standard deviation**	**Skewness**
$\boldsymbol{D_m}$	1.66	0.29	0.88	1.47	0.30	0.34
$\boldsymbol{\log_{10}(N_w)}$	3.86	0.23	-0.54	4.01	0.29	0.19
λ	10.08	5.22	1.29	13.15	7.49	1.09
μ	11.86	6.70	0.77	14.05	8.73	1.16

Table 5. Comparison of μ-λ relations derived in the present study with other orographic precipitation regions.

Study	**Climatic Regime**	μ-λ **relation**
Present study	Wet spells over WGs	$\lambda = 0.0359\ \mu^2 + 0.802\ \mu + 2.22$
Present study	Dry spells over WGs	$\lambda = 0.0138\ \mu^2 + 1.151\ \mu + 1.198$
Present study	Stratiform precipitation	$\lambda = 0.0022\ \mu^2 + 0.933\ \mu + 1.86$
Present study	Convective precipitation	$\lambda = 0.0069\ \mu^2 + 0.576\ \mu + 2.42$
Seela et al. (2018)	Summer season in Taiwan	$\lambda = 0.0235\ \mu^2 + 0.472\ \mu + 2.394$
Seela et al. (2018)	Winter season in Taiwan	$\lambda = -0.0135\ \mu^2 + 1.006\ \mu + 3.48$
Chen et al. (2017)	Summer season in Tibetan Plateau	$\lambda = -0.0044\ \mu^2 + 0.764\ \mu - 0.49$
Cao et al. (2008)	Oklahoma	$\lambda = -\ 0.02\ \mu^2 + 0.902\ \mu - 1.718$
Chu and Su (2008)	Typhoons in north Taiwan	$\lambda = 0.0433\ \mu^2 + 1.039\ \mu + 1.477$
Zhang et al. (2003)	Florida	$\lambda = 0.0365\ \mu^2 + 0.735\ \mu + 1.935$